

# GEOPHYSICS®

## INTERPRETATION OF BOREHOLE SONIC MEASUREMENTS ACQUIRED IN VTI FORMATIONS PENETRATED BY VERTICAL WELLS

Journal:	<i>Geophysics</i>
Manuscript ID	GEO-2017-0757.R1
Manuscript Type:	Technical Paper
Keywords:	bed thickness, borehole geophysics, elastic, frequency-domain, VTI
Area of Expertise:	Borehole Geophysics

SCHOLARONE™  
Manuscripts

**INTERPRETATION OF BOREHOLE SONIC MEASUREMENTS ACQUIRED IN VTI FORMATIONS PENETRATED BY VERTICAL WELLS**

**Authors:**

Elsa Maalouf, formerly with the University of Texas at Austin, currently with The American University of Beirut, em40@aub.edu.lb

Carlos Torres-Verdin, University of Texas at Austin, cverdin@austin.utexas.edu

Original paper date of submission: ----

Revised paper date of submission: ----

1  
2  
3  
4  
5  
6  
7  
8  
9  
10  
11  
12  
13  
14  
15  
16  
17  
18  
19  
20  
21  
22  
23  
24  
25  
26  
27  
28  
29  
30  
31  
32  
33  
34  
35  
36  
37  
38  
39  
40  
41  
42  
43  
44  
45  
46  
47  
48  
49  
50  
51  
52  
53  
54  
55  
56  
57  
58  
59  
60

## ABSTRACT

Detecting vertical transversely isotropic (VTI) formations and quantifying the magnitude of anisotropy are fundamental for describing organic mudrocks. Methods used to estimate stiffness coefficients of VTI formations often provide discontinuous or spatially averaged results over depth intervals where formation layers are thinner than the receiver aperture of acoustic tools. We introduce an inversion-based method to estimate stiffness coefficients of VTI formations that are continuous over the examined depth interval and that are mitigated for spatial averaging effects. To estimate the coefficients, we use logs of frequency-dependent compressional, Stoneley, and quadrupole/flexural modes measured with wireline or logging-while-drilling (LWD) instruments in vertical wells penetrating horizontal layers. First, we calculate the axial sensitivity functions of borehole sonic modes to stiffness coefficients; next, we use the sensitivity functions to estimate the stiffness coefficients of VTI layers sequentially from frequency-dependent borehole sonic logs. Because sonic logs exhibit spatial averaging effects, we de-average the logs by calculating layer-by-layer slownesses of formations prior to estimating stiffness coefficients. The method is verified with synthetic models of homogeneous and thinly-bedded formations constructed from field examples of organic mudrocks. Results consist of layer-by-layer estimates of  $c_{11}$ ,  $c_{13}$ ,  $c_{33}$ ,  $c_{44}$ , and  $c_{66}$ . We observe three sources of error in the estimated coefficients: (a) bias error originating from de-averaging the sonic logs prior to the sequential inversion, (b) error propagated during the sequential inversion, and (c) error associated with noisy slowness logs. We found that the relative bias and uncertainty of the estimated coefficients are largest for  $c_{11}$  and  $c_{13}$  because borehole modes exhibit low sensitivity to these two coefficients. The main advantage of our method is that it mitigates spatial averaging

effects of sonic logs while at the same time detects the presence of anisotropic layers and yields continuous estimations of stiffness coefficients along the depth interval of interest.

### INTRODUCTION

Detecting whether a rock formation is isotropic or vertical transversely isotropic (VTI) and estimating the associated stiffness coefficients of layers is important to quantify formation strength for drilling applications and production optimization.

Current borehole-based methods identify anisotropic formations by comparing shear slownesses measured with orthogonal dipole sources (fast and slow shear slownesses). However, these methods are not applicable to VTI formations penetrated with vertical wells because shear slownesses measured with orthogonal dipole sources are equal. Instead, anisotropic layers are typically identified by comparing the frequency-dependent flexural mode to the flexural slownesses calculated assuming an equivalent homogeneous and isotropic model described by density, compressional slowness, and shear slowness obtained from density, compressional, and low-frequency flexural logs, respectively. Differences in the frequency-dependent slownesses indicate that the formation is anisotropic; large differences indicate a high degree of anisotropy. However, this method does not consider the presence of heterogeneities in the formation, i.e., the effect of thin layers on the slownesses measured with acoustic tools (Peyret and Torres-Verdín, 2006). Furthermore, quantifying the degree of anisotropy requires the estimation of the stiffness coefficients of layers.

Walsh et al. (2006; 2007) introduced a procedure to determine stiffness coefficients of transversely isotropic (TI) formations using compressional, fast-shear, slow-shear, and Stoneley logs acquired in vertical and horizontal wells. Another method was introduced by Sinha et al.

1  
2  
3  
4  
5  
6  
7  
8  
9  
10  
11  
12  
13  
14  
15  
16  
17  
18  
19  
20  
21  
22  
23  
24  
25  
26  
27  
28  
29  
30  
31  
32  
33  
34  
35  
36  
37  
38  
39  
40  
41  
42  
43  
44  
45  
46  
47  
48  
49  
50  
51  
52  
53  
54  
55  
56  
57  
58  
59  
60

(2014; 2016) where multi-frequency flexural slownesses measured with wireline tools were used to extract stiffness coefficients of VTI formations. They calculated the sensitivity (derived from first-order perturbation) of the flexural velocity to stiffness coefficients and used the sensitivities at different frequencies to calculate stiffness coefficients. However, because sonic tools introduce spatial averaging effects on logs (Peyret and Torres-Verdín, 2006), the calculated coefficients with this method are averaged vertically over the length of the receiver array of wireline tools, which typically varies between 0.914 m (3 ft) and 1.828 m (6 ft) in length. Furthermore, it is expected that the flexural mode does not yield accurate estimates of the stiffness coefficients in formations logged with logging-while-drilling (LWD) instruments because flexural logs are affected by tool modes (Sinha et al., 2009), which bias the estimation of stiffness coefficients.

Assuming a vertical well penetrating horizontal layers, we develop an inversion-based algorithm to estimate stiffness coefficients of VTI formations using compressional, flexural/quadrupole, and Stoneley logs measured with wireline or LWD instruments. Because the formations are VTI, the elastic properties of each horizontal layer are entirely described by five independent stiffness coefficients, namely,  $c_{11}$ ,  $c_{13}$ ,  $c_{33}$ ,  $c_{44}$ , and  $c_{66}$  (and density). The inversion algorithm is performed in two steps: (1) reduction of spatial averaging effects on compressional, flexural/quadrupole, and Stoneley logs and calculation of layer-by-layer slownesses, and (2) estimation of the five stiffness coefficients from the calculated layer-by-layer slownesses. In the first step of the algorithm, we reduce the spatial averaging effects on logs within a few seconds of central processing unit (CPU) time using spatial sensitivity functions (Huang and Torres-Verdín, 2016). Hsu and Chang (1987) proposed an alternative method to reduce the spatial averaging effects on sonic logs using selective processing of receivers along the tool mandrel.

1  
2  
3 However, the latter procedure requires a minimum number of receivers to improve the  
4 processing resolution and signal-to-noise ratio (SNR). In the second step of the algorithm, we  
5 take advantage of the different sensitivities of borehole modes to stiffness coefficients and  
6 improve the robustness of the inversion by estimating the stiffness coefficients sequentially: first,  
7 we invert the compressional-wave log and the low-frequency Stoneley-wave log to calculate  $c_{33}$   
8 and  $c_{66}$ , respectively. Then, we invert the quadrupole/flexural log at low frequencies to calculate  
9  $c_{44}$ , and finally we invert the quadrupole/flexural logs at higher frequencies to calculate  $c_{11}$  and  
10  $c_{13}$ .

11  
12 We implement the method on synthetic examples to assess its reliability and accuracy  
13 under controlled conditions. Field data are not considered in the analysis and verification because  
14 multi-frequency dispersion curves (or waveforms) were not available for VTI formations.  
15 Furthermore, post-processed data and the geometries and elastic properties of the acoustic tool  
16 are needed to accurately implement the method.

17  
18 To construct the synthetic cases, we only consider homogeneous and horizontally layered  
19 formations penetrated by vertical wells, where the layers are thinner than the length of the  
20 receiver array (i.e., below 1.1 m). Each layer is intrinsically VTI, which means that each layer is  
21 described with five independent stiffness coefficients (or with Thomsen's parameters).  
22 Thomsen's parameters (Thomsen, 1986) vary within the range of values observed in Bakken and  
23 Barnett shales, i.e.,  $0.1 < \epsilon < 0.3$ ,  $0.09 < \gamma < 0.29$ , and  $0.04 < \delta < 0.11$  (Murphy et al., 2015; Tutuncu,  
24 2010; Vernik and Liu, 1997). The layer-by-layer stiffness coefficients obtained with the  
25 inversion method agree with the original coefficients with a relative bias below 7% for the  
26 estimated  $c_{33}$ ,  $c_{44}$ , and  $c_{66}$ , and can be as high as 17% for the estimated  $c_{11}$  and  $c_{13}$ . It is found  
27  
28  
29  
30  
31  
32  
33  
34  
35  
36  
37  
38  
39  
40  
41  
42  
43  
44  
45  
46  
47  
48  
49  
50  
51  
52  
53  
54  
55  
56  
57  
58  
59  
60

that when the layers are thinner than the length of the receiver array, the bias in the calculated coefficients increases because of spatial averaging effects. We calculate the standard deviation of the error of the estimated coefficients by adding zero-mean Gaussian noise to the slowness logs and find that the relative error in estimating  $c_{11}$  and  $c_{13}$  is the largest because borehole modes exhibit low sensitivity to these two coefficients. Therefore, in the presence of noisy measurements, alternative methods can be used to improve the estimations of  $c_{11}$  and  $c_{13}$ .

The inversion-based method is an efficient way (1) to reduce spatial averaging effects on sonic logs by quantifying the effect of beds thinner than the tool's receiver aperture on borehole acoustic logs, (2) to detect anisotropy and its magnitude, and (3) to calculate layer-by-layer values of  $c_{33}$ ,  $c_{44}$ , and  $c_{66}$  of VTI formations penetrated by vertical wells. Additionally, the method yields reliable estimates of  $c_{11}$  and  $c_{13}$  provided that the high-frequency components of flexural and quadrupole logs exhibit adequate SNR.

## METHOD

First, we calculate the first-order sensitivity of borehole sonic modes to the five stiffness coefficients  $c_{11}$ ,  $c_{13}$ ,  $c_{33}$ ,  $c_{44}$ , and  $c_{66}$ . Next, we calculate the axial averaging function introduced by acoustic instruments on borehole sonic logs. Finally, we describe the inversion-based algorithm used to mitigate spatial averaging effects on borehole sonic logs and to estimate the stiffness coefficients of layers.

### **Sensitivity function and forward model in a homogeneous formation**

In a homogeneous formation with a vector of elastic properties

$\mathbf{p}_0 = [c_{11}, c_{13}, c_{33}, c_{44}, \text{ and } c_{66}]$ , the sensitivity,  $S_k^{\{l\}}$ , of a sonic borehole mode  $\{l\}$  to the elastic property  $p_{0k}$  is given by

$$S_k^{\{l\}}(\mathbf{p}_0, f) = \frac{\partial s^{\{l\}}(\mathbf{p}_0, f)}{\partial p_{0k}}, \quad (1)$$

where  $s^{\{l\}}$  is the slowness of mode  $\{l\}$  at frequency  $f$  of a homogeneous formation whose stiffness coefficients are given by the vector  $\mathbf{p}_0$  and  $p_{0k}$  is the  $k$ -th stiffness coefficient. Figures 1 and 2 show the normalized sensitivity of the quadrupole and flexural modes calculated in slow and fast homogenous formations penetrated by LWD and wireline tools, respectively. The normalization factor is  $p_{0k}/s^{\{l\}}(\mathbf{p}_0, f)$ . Formation and borehole properties are given in Table 1, while the assumed tool properties are given in Table 2. The spatial sensitivities shown in Figures 1 and 2 are calculated with an extended receiver array to avoid spatial aliasing and improve spatial sampling (Foti et al., 2002). In subsequent sections,  $\{l\}$  is equal to  $\{q\}$  for quadrupole,  $\{fl\}$  for flexural,  $\{c\}$  for compressional, and  $\{st\}$  for Stoneley modes.

As a first-order approximation, the slowness  $s^{\{l\}}(\mathbf{p}, f)$  of a VTI homogeneous formation of elastic property  $\mathbf{p}$ , is expressed as

$$s^{\{l\}}(\mathbf{p}, f) = s^{\{l\}}(\mathbf{p}_0, f) + \sum_k S_k^{\{l\}}(\mathbf{p}_0, f)(p_k - p_{0k}), \quad (2)$$

where  $(p_k - p_{0k})/p_{0k} \ll 1$ .

### Sensitivity function and forward model in a layered (heterogeneous) formation

In a layered rock formation (rock formation with horizontal thin beds penetrated by a vertical borehole), the slowness of a sonic mode  $\{l\}$  measured by an acoustic tool is spatially

averaged along the borehole axis (Peyret and Torres-Verdín, 2006). The spatially averaged slowness  $\bar{s}^{\{l\}}(d, f)$  of a sonic mode  $\{l\}$  at frequency  $f$  measured by the tool at depth  $d$  is given by

$$\bar{s}^{\{l\}}(d, f) = \sum_{i=1}^N F(z_i - d) s^{\{l\}}(\mathbf{p}(z_i), f) + O(s^2), \quad (3)$$

where  $s^{\{l\}}(\mathbf{p}(z_i), f)$  is the slowness of the homogeneous formation of elastic properties  $\mathbf{p}$  at depth  $z_i$ , that is midway between receivers  $i$  and  $i + 1$  (see Figure 3), and  $F$  is a spatial averaging function that depends on the tool *geometrical* properties. We assume that higher-order terms contributing to the spatially averaged slowness are negligible; therefore, substitution of equation 2 into equation 3 yields

$$\bar{s}^{\{l\}}(d, f) = \sum_{i=1}^N F(z_i - d) \left[ s^{\{l\}}(\mathbf{p}_0(z_i), f) + \sum_k S_k^{\{l\}}(\mathbf{p}_0(z_i), f) (p_k(z_i) - p_{0k}(z_i)) \right], \quad (4)$$

$$\begin{aligned} \bar{s}^{\{l\}}(d, f) &= \sum_{i=1}^N F(z_i - d) s^{\{l\}}(\mathbf{p}_0(z_i), f) \\ &+ \sum_{i=1}^N \sum_k F(z_i - d) S_k^{\{l\}}(\mathbf{p}_0(z_i), f) (p_k(z_i) - p_{0k}(z_i)), \end{aligned} \quad (5)$$

and

$$\bar{s}^{\{l\}}(d, f) = \bar{s}_0^{\{l\}}(d, f) + \sum_{i=1}^N \sum_k F(z_i - d) S_k^{\{l\}}(\mathbf{p}_0(z_i), f) (p_k(z_i) - p_{0k}(z_i)), \quad (6)$$

where  $\{l\}$  denotes the sonic mode,  $\bar{s}_0^{\{l\}}(d, f)$  is the average slowness of the reference homogeneous background between the first and  $N$ -th receivers of the acoustic tool,  $z_i = d + L/2 - (i - 1/2)L/(N - 1)$  (see Figure 3),  $L$  is the length of the receiver array, and  $p_k(z_i)$  is the value of rock property  $p_k$  at depth  $z_i$ . The forward model is expressed as a function of the

product of  $F$  and  $S$ . Therefore, the effects of spatial averaging on logs (given by  $F$ ) and of the sensitivity of a borehole mode to the stiffness coefficients (given by  $S$ ) can be decoupled to calculate sonic logs.

Equation 6 is similar to the forward model proposed by Huang et al. (2015) to calculate sonic logs in horizontally layered formations given by

$$s^{\{l\}}(d, f) = s^{\{l\}}(\mathbf{p}_0, d, f) + \sum_z \sum_k \frac{p_k(z) - p_{0k}(d)}{p_{0k}(d)} G^{\{l\}}(p_{0k}, z, f) s^{\{l\}}(\mathbf{p}_0, d, f), \quad (7)$$

where  $G^{\{l\}}(p_{0k}, z, f)$  is the normalized axial sensitivity function of the sonic mode  $\{l\}$  to elastic property  $p_{0k}$  (a detailed explanation on the method used to calculate  $G$  is given in the Appendix).

By comparing equations 6 and 7, we find that

$$G^{\{l\}}(p_{0k}, z, f) \frac{s^{\{l\}}(\mathbf{p}_0, f)}{p_{0k}(z)} = F(z) S_k^{\{l\}}(\mathbf{p}_0(z), f). \quad (8)$$

Furthermore,  $S$  depends on the borehole fluid, tool's elastic properties, sonic mode, frequency, and rock elastic properties, and is given by equation 1, while  $F$  is an analytical expression that depends on the tool's *geometrical* properties and can be calculated using ray theory. Maalouf and Torres-Verdín (2017) showed that

$$F(z_i) = \frac{s(z_i) - s_r}{s_p - s_r}, \quad (9)$$

where  $s_r$  is the slowness of a reference homogeneous formation and  $s(z_i)$  is the slowness measured by the sonic tool when a layer (layer  $Y$ ) of slowness  $s_p$  and thickness  $\Delta z_L$  is inserted

and centered at depth  $z_i$  between two consecutive receivers  $i$  and  $i + 1$  of the sonic tool. The measured slowness,  $s(z)$ , at the  $N$  receivers of the tool is given by

$$s(z) = \frac{T}{D_T}, \quad (10)$$

where  $D_T$  is the total distance traveled by the wave and  $T$  is total travel time. Total travel time is calculated by adding the travel time it takes the borehole wave to propagate from one receiver to another, for all possible combinations of receiver pairs, which yields

$$s(z_i) = \frac{\frac{1}{6} s_r N(N^2 - 1) + (s_p - s_r) i(N - i)}{\frac{1}{6} N(N^2 - 1)}. \quad (11)$$

Substitution of equation 11 into equation 9 gives

$$F(z_i) = \begin{cases} \frac{6i(N - i)}{N(N^2 - 1)} & \text{for } z_i \text{ between receivers } i \text{ and } i+1, \\ 0 & \text{for } z_i \text{ outside the receiver array,} \end{cases} \quad (12)$$

where  $i = 1, 2, \dots, (N - 1)$ . Figure 3 shows the geometry and the position of the receivers while Figure 4 describes  $F$  for the LWD and wireline tools given in Table 2.

We show in the Appendix that the relative difference between  $G$  (equation 7) normalized by  $\frac{s^{\{l\}}(\mathbf{p}_0, f)}{p_{ok}(z)}$  and the product of  $F$  (equation 12) by  $S$  (equation 1) is within 1%, which confirms that the second-order terms in equation 3 are negligible. By substituting equation 12 into equation 3, we obtain the forward model of sonic logs in a layered formation, given by

$$\bar{s}^{\{l\}}(d, f) = \sum_{i=1}^N \frac{6i(N - i)}{N(N^2 - 1)} s^{\{l\}}(\mathbf{p}(z_i), f), \quad (13)$$

where  $s^{\{l\}}(\mathbf{p}(z_i), f)$  is the slowness of mode  $\{l\}$  at frequency  $f$  of the homogeneous formation with elastic properties  $\mathbf{p}$  at depth  $z_i = d + L/2 - (i - 1/2) L/(N - 1)$ ,  $N$  is total number of receivers, and  $s^{\{l\}}$  is calculated using one-dimensional (1D) simulations of borehole modes (Tang and Cheng, 2004).

### Inversion algorithm

We perform inversion-based interpretation of borehole sonic logs in two steps: in the first step, we mitigate spatial averaging effects on the borehole sonic logs to obtain layer-by-layer slownesses of formations, while in the second step we estimate stiffness coefficients from the calculated layer-by-layer slownesses.

#### *Inversion Step 1*

In *Step 1* of the inversion method, we mitigate spatial averaging effects on frequency-dependent (dispersive) and non-dispersive (compressional) sonic logs introduced by acoustic instruments when layers are thinner than the tool's receiver aperture. To mitigate spatial averaging effects, we calculate layer-by-layer slownesses by minimizing the quadratic cost function given by

$$e_1(\mathbf{m}(f_i)) = \|\mathbf{F}\mathbf{m}(f_i) - \mathbf{d}_{\log}(f_i)\|_2^2 + \alpha^2 \|\mathbf{W}_n \cdot \mathbf{m}(f_i)\|_2^2, \quad (14)$$

at each frequency  $f_i$ , where  $\mathbf{m}(f_i)$  is the model vector whose components  $m_k(f_i)$  are the slownesses at depth  $z_k$  and frequency  $f_i$ ;  $\mathbf{d}_{\log}(f_i)$  is the data vector whose components  $(d_{\log}(f_i))_j$  is the slowness log at frequency  $f_i$  and measured depth  $d_j$  ( $z$  denotes any position in the formation,  $d$  denotes depth of the log), and  $F_{jk} = F(z_k - d_j)$  is the value of the spatial

averaging function at position  $z_k$  when the receiver array is centered at depth  $d_j$ . The second additive term of the cost function (equation 14) is a Tikhonov regularization (stabilization) term, where  $\alpha$  is the regularization parameter and  $\mathbf{W}_n$  is a regularization weighting matrix; when layers are thicker than the full width at half maximum of the function  $F$  we do not implement regularization, i.e., we set  $\alpha = 0$ . The full width at half maximum is the length of the interval that verifies  $F < \frac{\max(F)}{2}$ , where  $\max(F)$  is the maximum value of the function  $F$ ;  $\max(F)$  is reached at the center of the receiver array (see Figure 4).

Bed boundaries and the initial guess of model properties are input to the inversion as follows:

- In synthetic cases, the locations of bed boundaries are known while for field data they are estimated from other well logs (e.g., gamma ray, density, or resistivity).
- The initial guess of the model properties for each layer is chosen as the mean value of the corresponding well log (e.g., density, slowness) across that layer.

To minimize the quadratic cost function (equation 14), we use the Levenberg-Marquardt method (Aster et al., 2005). In the examples considered in this paper we do not use regularization; thus,  $\alpha = 0$  and the gradient of the cost function becomes

$$\frac{\partial e_1(\mathbf{m}(f_q))}{\partial m_k} = \frac{\partial \left\| F(z_j - d_i)m_j(f_q) - (d_{\log}(f_q))_i \right\|_2^2}{\partial m_k}, \quad (15)$$

where  $f_q$  is frequency,  $(d_{\log})_i$  is the slowness data at measured depth  $d_i$ , and  $m_j$  is the slowness of the layer at depth  $z_j$ . Simplifying equation 15 yields

$$\frac{\partial e_1(\mathbf{m}(f_q))}{\partial m_k} = 2 \left( F_{ij} m_j(f_q) - (d_{\log}(f_q))_i \right) F_{ik}, \quad (16)$$

whereby the entries of the Jacobian matrix  $\mathbf{J}$  are given by  $J_{ij} = F_{ij} = F(z_j - d_i)$ .

### *Inversion Step 2*

In *Step 2* of the inversion method, we calculate stiffness coefficients of layers from the layer-by-layer, frequency-dependent slownesses obtained in *Step 1*. This is accomplished by minimizing the quadratic cost function given by

$$e_2(\mathbf{p}_k) = \|\mathbf{g}(\mathbf{p}_k) - \mathbf{s}_k\|_2^2, \quad (17)$$

separately for each layer  $k$ , where  $\mathbf{p}_k$  is the model vector of layer  $k$  whose entries are the five stiffness coefficients,  $\mathbf{s}_k$  is the slowness vector at all frequencies  $f_q$  in a given layer  $k$ ; i.e.,  $(s_q)_k = m_k(f_q)$ , ( $\mathbf{m}$  is defined in equation 14) and  $\mathbf{g}(\mathbf{p}_k)$  is the modeled slowness vector calculated using 1D simulations. To minimize the quadratic cost function (equation 17), we use the Levenberg-Marquardt method (Aster et al., 2005) and calculate the entries of the corresponding Jacobian matrix using 1D simulations.

To improve the efficiency of the inversion, we implement equation 17 in the following way: First, we use the compressional mode to estimate  $c_{33}$  from  $c_{33} = v_{pv}^2 \rho$ , where  $v_{pv}$  is the vertical compressional velocity obtained from the compressional log and  $\rho$  is rock density (known or obtained from the density log). Next, we use the Stoneley mode at low frequencies to calculate  $c_{66}$  given that  $S_k^{\{st\}}(\mathbf{p}_0, f < f_{st\_cutoff}) \approx 0$  for all  $p_{0k}$  except  $c_{66}$  where  $f_{st\_cutoff}$  is the Stoneley cut-off frequency (Tang and Cheng, 2004). Next, we use the low-frequency component of the flexural/quadrupole modes to estimate  $c_{44}$  given that  $S_k^{\{fl\}}(\mathbf{p}_0, f \leq$

$f_{fl\_cutoff} \approx 0$  and  $S_k^{\{q\}}(\mathbf{p}_0, f \leq f_{q\_cutoff}) \approx 0$  for all  $p_{0k}$  except  $c_{44}$  (see Figures 1 and 2) where  $f_{fl\_cutoff}$  and  $f_{q\_cutoff}$  are the flexural and quadrupole cut-off frequencies, respectively. Finally, we invert the flexural/quadrupole log at higher discrete frequencies to estimate  $c_{11}$  and  $c_{13}$  because the ratios  $S_{c_{44}}^{\{fl\}}(\mathbf{p}_0, f)/S_{c_{33} \text{ or } c_{13}}^{\{fl\}}(\mathbf{p}_0, f)$  and  $S_{c_{44}}^{\{q\}}(\mathbf{p}_0, f)/S_{c_{33} \text{ or } c_{13}}^{\{q\}}(\mathbf{p}_0, f)$  decrease when frequency increases. For the Stoneley mode the cut-off frequency is defined as the frequency below which the slowness becomes relatively constant, while for the flexural and quadrupole mode the cut-off frequency is reached when the slowness is equal to the formation shear slowness.

In all the examples, the sequential inversion is initialized assuming that each layer in the formation earth model is isotropic, i.e., completely described using density,  $c_{44}$ , and  $c_{33}$ . During inversion, we update the earth model to account for the effects of anisotropy (VTI) on the measured slowness whereby each layer is described by  $c_{11}$ ,  $c_{13}$ ,  $c_{33}$ ,  $c_{44}$ , and  $c_{66}$ . The description of the inversion procedure (*Step 2*) is given in Table 3. We use a total of 14 well logs to perform the sequential inversion, as follows:

- One compressional log (to estimate  $c_{33}$ ).
- One Stoneley log (to estimate  $c_{66}$ ). The frequency is determined from the Stoneley dispersion curve at the lowest frequency with constant slowness, usually between 1 kHz and 2 kHz.
- One flexural/quadrupole log at low frequency (to estimate  $c_{44}$ ). For the flexural mode, the frequency is chosen at the point where the dispersion curve asymptotes to a constant value, usually between 2 kHz and 3 kHz. For the quadrupole mode, the low frequency is chosen around the cut-off frequency at approximately 3.5 kHz for

slow/intermediate formations and 4.5 kHz for fast formations (Su et al., 2013; Matuszyk and Torres-Verdín, 2014).

- Eleven discrete frequencies from 4.5 kHz to 7 kHz (to estimate  $c_{11}$  and  $c_{13}$ ).

Although we use discrete frequencies for the inversion, continuous frequencies can be used if the measurement is noisy to increase the SNR. The sampling depth interval of well logs is 0.1524 m (0.5 ft).

### RESULTS

We apply the inversion method to three synthetic examples logged with LWD instruments. Synthetic quadrupole, Stoneley, and P-wave slownesses are generated using two-dimensional finite-element (2DFE) (Matuszyk et al., 2014) and finite-difference (2DFD) (Peyret and Torres-Verdín, 2006; Xu et al., 2005) numerical simulations. In Example 1, we use sequential inversion to estimate the stiffness coefficients of a homogeneous formation. Example 2 includes a thin layer within the homogeneous formation with the intent of showing how the spatial averaging effects intrinsic to sonic logs can bias the estimated coefficients. Example 3 applies the method to a fast formation that includes high degree of anisotropy, thin layers, and large contrast of elastic properties between adjacent layers with the intent of examining the effects of spatial averaging of sonic logs and formation type on the estimated coefficients. In all the examples, Thomsen’s parameters of the layers are chosen within the ranges:  $0.1 < \epsilon < 0.3$ ,  $0.09 < \gamma < 0.29$ , and  $0.04 < \delta < 0.11$ . Table 4 describes the synthetic examples and summarizes the parameters used for inversion (i.e., frequency, number of logging points, type of tool, and type of formation).

#### Example 1 – Homogeneous formation

1  
2  
3  
4  
5  
6  
7  
8  
9  
10  
11  
12  
13  
14  
15  
16  
17  
18  
19  
20  
21  
22  
23  
24  
25  
26  
27  
28  
29  
30  
31  
32  
33  
34  
35  
36  
37  
38  
39  
40  
41  
42  
43  
44  
45  
46  
47  
48  
49  
50  
51  
52  
53  
54  
55  
56  
57  
58  
59  
60

First, we consider the simple case of a homogeneous VTI formation logged with an LWD instrument to validate the inversion workflow followed in the estimation of stiffness coefficients (*Step 2*, Table 3). Figure 5 shows the frequency-dependent slowness and the stiffness coefficients of the formation in black, of the initial guess in blue, and of the estimations in red. The difference between actual and inverted coefficients,  $e$ , varies between 0.03 GPa and 1.14 GPa (equivalent to 0.3% and 9% relative error, respectively);  $e$  is largest for  $c_{13}$  because the quadrupole mode exhibits low sensitivity to this coefficient (see Figure 1).

We conclude that the proposed method accurately estimates  $c_{11}$ ,  $c_{33}$ ,  $c_{44}$ , and  $c_{66}$  in a homogeneous formation with noise-free measurements which are also devoid of spatial averaging effects, and that the estimation of  $c_{13}$  is biased because of the low measurement sensitivity.

### Example 2 – Layered formation

The objective of this example is (1) to validate the inversion workflow to mitigate spatial averaging effects on well logs (*Step 1*) and (2) to show the effect of spatial averaging and measurement noise on the estimated coefficients. Therefore, we include a thin layer within the homogeneous formation of Example 1. The total log interval is 3 m, corresponding to 21 logging points. Figure 6 shows the frequency-dependent, synthetic borehole sonic logs in black and the true layer-by-layer slownesses with black dashed lines. Spatial averaging effects on the synthetic borehole logs are mitigated by applying *Step 1* of the inversion method and calculating layer-by-layer slownesses (blue dashed lines). Error bars superimposing the logs were calculated by adding zero-mean Gaussian noise with 0.4  $\mu\text{s}/\text{ft}$  standard deviation to the input logs (blue circles) and applying the inversion method 50 times with the same initial guess but different instances of

noise. Error bars indicate the 95% confidence interval of inverted slownesses (Figure 6). Each inversion (*Step 1*) converges in less than 5 iterations and is completed within a few seconds of CPU time.

We use the value of the inverted frequency-dependent quadrupole, Stoneley, and compressional slownesses (blue dashed lines) of each layer, individually, to calculate stiffness coefficients using the method described in Table 3. Figure 7 shows the estimated  $c_{11}$ ,  $c_{13}$ ,  $c_{33}$ ,  $c_{44}$ , and  $c_{66}$  with blue dashed lines while Table 4 summarizes the parameters used for inversion. The distribution of the error of the estimated stiffness coefficients shows a bias, caused by both the de-averaging process and the propagation of error on the stiffness coefficients during sequential inversion. The standard deviation of the error distribution of the stiffness coefficients,  $\sigma_{c_k}$ , depends on the standard deviation of the measured slowness,  $\sigma_s$ , where  $k=1, 2, \dots, 5$  and  $c_k$  is the  $k$ -th stiffness coefficient of the vector  $[c_{11}, c_{13}, c_{33}, c_{44}, c_{66}]$ . As a first-order approximation, we can quantify the error,  $\Delta c_k$ , in estimating stiffness coefficient  $c_k$  in terms of the errors,  $\Delta s(f_i)$ , of the estimated slowness  $s$  at frequency  $f_i$  using equation 2:

$$\Delta s(f_i) = \sum_k S_k(f_i) \Delta c_k, \quad (18)$$

where  $S_k$  is the sensitivity of mode slowness to  $c_k$  and is given by equation 1. Writing equation 18 in matrix form, we obtain

$$\Delta \mathbf{s} = \mathbf{S} \Delta \mathbf{c}. \quad (19)$$

An error in  $\Delta \mathbf{s}$  can be propagated to an error in  $\Delta \mathbf{c}$  using the covariance matrix  $\mathbf{cov}(\Delta \mathbf{c})$ . The standard deviations of the stiffness coefficients are approximated from the diagonal elements of  $\mathbf{cov}(\Delta \mathbf{c})$ , which is given by (Aster et al., 2005):

$$\mathbf{cov}(\Delta \mathbf{c}) = (\mathbf{S}^t \mathbf{\Sigma}^2 \mathbf{S})^{-1}, \quad (20)$$

where  $S_{ij} = S_j(f_i)$ ,  $\Sigma_{ij} = \text{diag}(1/\sigma_{s(f_i)})$ ,  $\sigma_{s(f_i)}$  is the standard deviation of the error of the inverted slowness at frequency  $f_i$  (obtained from *Step 1*), and the superscript  $t$  denotes matrix transpose. The standard deviation,  $\sigma_{c_k}$ , of the error of the estimated coefficient  $c_k$  is given by

$$\sigma_{c_k} = (\mathbf{S}^t \mathbf{\Sigma}^2 \mathbf{S})_{kk}^{-1}. \quad (21)$$

The columns ‘Data’ and ‘Coefficient to Estimate’ of Table 3 define  $\mathbf{s}$  and  $\mathbf{c}$ , respectively, for every step of the sequential inversion. In Figure 7, errors bars indicate the 95% confidence interval of the estimated coefficients (equal to  $3.92\sigma_{c_k}$ ). Table 5 describes the relative bias and the maximum standard deviation of the error for the estimated coefficients. Larger error bars and misfits are observed for the estimations of  $c_{11}$  and  $c_{13}$  compared to  $c_{44}$  because the sensitivity of the quadrupole mode to  $c_{11}$  and  $c_{13}$  is low (Figure 1).

### Example 3 – Fast heterogeneous formation

In this example, we show that in general (1) spatial averaging biases the estimated coefficients, (2) sequential inversion provides better estimates of stiffness coefficients than simultaneous inversion, and (3) de-averaging the well logs prior to inversion improves the estimation of coefficients.

We construct a synthetic model with a degree of slowness anisotropy varying between 0.05% and 17%. Layer thicknesses are smaller than the length of the receiver array while the difference between the shear slowness of adjacent layers is on average 22  $\mu\text{s}/\text{ft}$ . The sampling interval is 0.1524 m (0.5 ft), and the depth interval is 11 m (69 logging points). Because the layers are thin and the slowness contrast between consecutive layers is large, sonic logs suffer from spatial averaging. We mitigate spatial averaging by applying *Step 1* of the inversion-based method. Figure 8 shows the inverted frequency-dependent slownesses in blue, while the error bars superimposing the logs are calculated by adding zero-mean Gaussian noise with 0.4  $\mu\text{s}/\text{ft}$  standard deviation to the modeled logs and applying the inversion method 50 times with the same initial guess but different instances of noise. Results confirm that de-averaging the well logs improves the estimation of slownesses in the vicinity of layer boundaries.

We estimate the stiffness coefficients using sequential and simultaneous inversion and calculate the ratio of relative errors. Figure 9 shows the estimated stiffness coefficients (blue dashed lines) from the sequential inversion (*Step 2*), where error bars indicate the 95% confidence interval of the estimations. Table 5 summarizes the maximum relative bias and the standard deviation of the estimated coefficients. Figure 10 compares the estimated coefficients from the sequential inversion (blue dashed lines) and the simultaneous (green dashed lines) inversion obtained using 11 quadrupole logs at discrete frequencies between 4.5 kHz and 7 kHz while Table 6 summarizes the ratio of the relative errors. The average ratio is larger than 1 for the estimated  $c_{11}$  and  $c_{13}$ . Therefore, in general, the sequential inversion procedure improves the estimation of  $c_{11}$  and  $c_{13}$  compared to simultaneous inversion because the sensitivity of the quadrupole mode to  $c_{44}$  at  $f > 4.5$  kHz is 2 to 4 times larger than the sensitivity to  $c_{11}$  and  $c_{13}$  (Figure 1).

To show the impact of de-averaging well logs prior to inversion, we estimate the stiffness coefficients with and without de-averaging and calculate the ratio of relative errors. Figure 10 shows the estimated coefficients (red dots) obtained when we invert the slowness of the input well logs at the center of each layer. Table 7 summarizes the ratio of the relative errors and shows that the average value of the ratio is  $> 1$ . Therefore, de-averaging well logs prior to inversion improves the estimation of coefficients to more accurately reproduce the actual elastic properties of the formations. However, in this example, the average ratio remains smaller than 1 for the estimation of  $c_{11}$  because of biasing introduced by the sequential inversion.

## DISCUSSION

### Detecting anisotropy in vertical wells

A conventional method used to detect anisotropy in rock formations logged with acoustic wireline tools is to compare the flexural slownesses measured with orthogonal dipoles; differences between the flexural slownesses measured with orthogonal dipoles can indicate the presence of elastic anisotropy. However, flexural slownesses measured at low frequencies with orthogonal dipoles are equal in VTI formations penetrated by vertical wells; fast shear slownesses equal slow shear slownesses (Sinha et al., 1994) even if the layers are VTI. Therefore, a formation drilled with a vertical well and exhibiting equal fast and slow shear slownesses is either isotropic or VTI.

We propose an alternative workflow to detect VTI anisotropy in layers penetrated by vertical wells. First, we calculate flexural logs assuming that the formation is isotropic; the parameters needed for that are rock density,  $c_{44}$ , and  $c_{33}$  that we obtain from the density log, the low-frequency flexural log, and the compressional log, respectively. Next, we analyze the data

1  
2  
3 residuals between the calculated and measured flexural slownesses. A bias in data residuals will  
4  
5 indicate that the formation is anisotropic.  
6  
7

8  
9 We apply the above workflow to the formation described in Example 2 logged with a  
10  
11 wireline tool. A dipole source is used to acquire the flexural logs while a monopole source is  
12  
13 used to acquire the compressional, and Stoneley logs. Figure 11 shows the input frequency-  
14  
15 dependent sonic logs and the inverted layer-by-layer slownesses obtained from *Step 1* of the  
16  
17 inversion method. First, we assume that the formation is isotropic and estimate  $c_{44}$ , and  $c_{33}$  from  
18  
19 the low-frequency flexural and compressional slownesses, respectively; next, we forward model  
20  
21 the flexural logs. Figure 12a compares the input flexural logs (synthetic logs) to the modeled  
22  
23 flexural logs while Figure 12b shows the histogram of data residuals between input and modeled  
24  
25 flexural logs. The histogram shows a biased distribution of data residuals, thereby indicating that  
26  
27 the formation is not isotropic. Therefore, to reduce biases in data residuals, we perform the  
28  
29 inversion assuming that the formation is VTI. We estimate the five stiffness coefficients using  
30  
31 *Step 2* of the inversion-based method. Figure 13a compares the input flexural logs to the flexural  
32  
33 logs calculated from the inversion while Figure 13b shows the histogram of data residuals. The  
34  
35 histogram approximates a Gaussian distribution centered at zero and has a 95% confidence  
36  
37 interval of 1.46  $\mu\text{s}/\text{ft}$ ; it is therefore concluded that the formation is better described with VTI  
38  
39 layers.  
40  
41  
42  
43  
44  
45  
46  
47  
48  
49  
50  
51  
52  
53  
54  
55  
56  
57  
58  
59  
60

61  
62 Figure 14 shows the estimated stiffness coefficients obtained from *Step 2* of the inversion  
63  
64 method while Table 5 describes the maximum relative bias and the standard deviation of the  
65  
66 error in the estimated coefficients (Example 4 in Table 5).

We conclude that the analysis of data residuals can be used to detect anisotropy in formations. However, it is remarked that in practice a biased distribution of data residuals could also indicate the presence of features not accounted for in the model such as orthorhombic anisotropy, dipping layers, washout, breakouts, or fractures, among others.

### Limitations and uncertainty of inverted coefficients

In the synthetic examples described above, we showed that the error in estimating  $c_{11}$  and  $c_{13}$  is larger than the error in estimating  $c_{33}$ ,  $c_{44}$ , and  $c_{66}$ , for two main reasons: first, the sensitivity of the quadrupole/flexural modes to  $c_{11}$  and  $c_{13}$  is low (Figures 1 and 2); therefore, small errors in the slowness (data) yield large errors in the estimated  $c_{11}$  and  $c_{13}$  (we quantified this type of error by calculating the 95% confidence interval shown in Figures 7, 9, and 14); second, because we use sequential inversion to estimate the stiffness coefficients, the errors in the estimation of  $c_{44}$ ,  $c_{66}$ , and  $c_{33}$  will propagate to and reduce the accuracy of the estimated  $c_{11}$  and  $c_{13}$  (we quantified this type of error by calculating the relative bias between actual and inverted coefficients in Table 5).

We use sequential and not simultaneous inversion to estimate stiffness coefficients because flexural/quadrupole slownesses exhibit low sensitivity to  $c_{11}$  and  $c_{13}$  at low frequencies. Using simultaneous inversion would introduce larger uncertainties on  $c_{11}$  and  $c_{13}$ , especially in the presence of noisy slowness measurements. In the presence of noisy slowness measurements, rock-physics constraints can be included in the estimation of stiffness coefficients, e.g.,  $\gamma > 0$ ,  $\varepsilon - \delta > 0$ ,  $\delta \leq (2/(c_{33}/c_{44} - 1))$ , and  $\delta \geq -1/2(1 - c_{44}/c_{33})$  where  $\varepsilon$ ,  $\gamma$ , and  $\delta$  are Thomsen's parameters (Yan et al., 2016; Berryman et al., 1999; Thomsen, 1986; Spikes, 2014).

The method assumes that bed-boundary locations are known. Errors in the location of bed boundaries can induce errors in *Step 1* of the inversion method. If the locations of bed boundaries are not known, beds can be positioned to coincide with log-sampling points. Because layer thicknesses (dictated by the log-sampling points) are smaller than the full width at half maximum of the axial sensitivity function, stabilization is required for the inversion (i.e.,  $\alpha > 0$ ). However, inverted logs will approach the measured (data) logs (Maalouf and Torres-Verdín, 2018); therefore, applying *Step 2* with bed boundaries aligned with log-sampling point is equivalent to applying the method on the measurements slowness, as we showed in Example 3 (see red dots in Figure 10).

Additional sources of errors unaccounted for in this paper are the presence of near-wellbore damage or washouts that impact the flexural and quadrupole modes at high frequencies. Furthermore, the method assumes that the density and velocity of the borehole fluid are known beforehand. Uncertainties in the velocity of the borehole fluid induce errors in the estimated  $c_{66}$  from the Stoneley log.

Finally, the proposed inversion method is only applicable to slowness measurements acquired in vertical wells penetrating horizontal layers; it remains to be examined whether small layer dips could have a measurable impact on the estimated coefficients. The method can be applied to horizontal transversely isotropic formations provided that the formation is drilled with a horizontal well that is perpendicular to the formation's isotropy plane.

### Calculating shear slownesses from quadrupole logs

Calculating shear slownesses (or  $c_{44}$ ) from quadrupole logs is challenging because the low-frequency components of the quadrupole mode are smaller than the true formation shear

1  
2  
3  
4  
5  
6  
7  
8  
9  
10  
11  
12  
13  
14  
15  
16  
17  
18  
19  
20  
21  
22  
23  
24  
25  
26  
27  
28  
29  
30  
31  
32  
33  
34  
35  
36  
37  
38  
39  
40  
41  
42  
43  
44  
45  
46  
47  
48  
49  
50  
51  
52  
53  
54  
55  
56  
57  
58  
59  
60

slowness (Scheibner et al., 2010). Figure 15 shows the synthetic quadrupole logs of Examples 2 and 3 where we superimpose the true layer shear slownesses in black. The low-frequency quadrupole slowness does not asymptote to shear slowness, hence cannot be used to reliably estimate  $c_{44}$ . Therefore, we calculate the shear slowness ( $ss_v$ ) from  $ss_v = \sqrt{\rho/c_{44}}$ , where  $c_{44}$  is estimated from *Step 2* of the inversion method (see estimated  $c_{44}$  in Figures 7 and 9). Figure 15 shows the values of  $ss_v$  in red where the relative estimation error is within 3%. Therefore, the inversion-based method can be used to estimate layer-by-layer shear slownesses from the low-frequency quadrupole slowness.

## CONCLUSIONS

We showed that forward modeling and inversion of frequency-dependent borehole sonic logs measured with wireline and logging-while-drilling (LWD) tools could be used to detect formation anisotropy and calculate the stiffness coefficients of vertical transversely isotropic (VTI) layers. It was verified that the inversion-based interpretation method yields accurate estimations of  $c_{33}$ ,  $c_{44}$ , and  $c_{66}$  in VTI formations while reducing the spatial averaging effects on slowness logs. Inversion results exhibit larger uncertainties when estimating  $c_{11}$  and  $c_{13}$  because the sensitivity of the sonic modes to these two coefficients is low. However, when the measurements are noise-free and mitigated for spatial averaging effects, the inversion method yields reliable estimates for  $c_{11}$  and  $c_{13}$ .

To mitigate spatial averaging effects on sonic logs, we use an analytical spatial averaging function ( $F$ ) to forward model sonic logs in a few seconds of CPU time. Additionally, the method estimates layer-by-layer shear slownesses from quadrupole logs whereby the estimated stiffness coefficients are available across the entire depth interval of study.

The method assumes VTI horizontally layered formations penetrated by vertical wells, neglecting radial heterogeneities (e.g., invasion and drilling damage). Presence of noise or radial heterogeneities will impact the estimation of stiffness coefficients because dispersive modes are sensitive to near-borehole properties.

**ACKNOWLEDGMENTS**

The work reported in this paper was funded by the University of Texas at Austin’s Research Consortium on Formation Evaluation, jointly sponsored by AkerBP, Anadarko, Aramco, Baker-Hughes, BHP Billiton, BP, China Oilfield Services LTD., Chevron, ConocoPhillips, DEA, ENI, Halliburton, Hess, Inpex, Lundin-Norway, Nexen, Petrobras, Repsol, Shell, Southwestern, Statoil, TOTAL, Wintershall, and Woodside Petroleum Limited. Carlos Torres-Verdin is grateful for the financial support provided by the Brian James Jennings Memorial Endowed Chair in Petroleum and Geosystems Engineering.

**APPENDIX**

**CALCULATION OF SONIC AXIAL SENSITIVITY FUNCTIONS**

We first describe how to calculate the axial sensitivity  $G^{\{l\}}$  used by Huang et al. (2015); next we compare  $G^{\{l\}}$  to the normalized product of  $F$  and  $S^{\{l\}}$  (equations 1 and 12) in a VTI formation penetrated by LWD and wireline tools. Finally, we show that the sensitivities calculated using both equations agree within a relative difference of 1%.

Huang et al. (2015) showed that the normalized frequency-domain axial sensitivity function of a sonic mode  $\{l\}$  at frequency  $f$  of a homogeneous formation of elastic properties  $\mathbf{p}_0$  to perturbations of elastic property  $p_{0k}$  is given by

1  
2  
3  
4  
5  
6  
7  
8  
9  
10  
11  
12  
13  
14  
15  
16  
17  
18  
19  
20  
21  
22  
23  
24  
25  
26  
27  
28  
29  
30  
31  
32  
33  
34  
35  
36  
37  
38  
39  
40  
41  
42  
43  
44  
45  
46  
47  
48  
49  
50  
51  
52  
53  
54  
55  
56  
57  
58  
59  
60

$$G^{\{l\}}(p_{0k}, z, f) = \frac{(s^{\{l\}}(z, f) - s^{\{l\}}(\mathbf{p}_0, f))/s^{\{l\}}(\mathbf{p}_0, f)}{(p_k - p_{0k})/p_{0k}}, \quad (\text{A-1})$$

where  $s^{\{l\}}(\mathbf{p}_0, f)$  is the slowness of a homogeneous reference background of elastic properties  $\mathbf{p}_0$ . In equation A-1,  $s^{\{l\}}(z, f)$  is the slowness measured by the sonic tool when a horizontal layer (layer  $Y$ ) of elastic property  $p_k \neq p_{0k}$  and thickness  $\Delta z_L$  is inserted at depth  $z$  between two consecutive receivers of the sonic tool in the presence of a reference homogeneous formation. To calculate  $G^{\{l\}}$  at every position  $z$ , layer  $Y$  is shifted in the vertical direction across the receiver array of the tool. For every position of layer  $Y$ , we calculate the spectrum of the wave mode  $\{l\}$  registered by the receivers of the tool and process the spectrum to obtain the slowness  $s^{\{l\}}(z, f)$ . In what follows, we show how to calculate the spectrum analytically in a 1D medium using boundary conditions of displacement and stress at the boundaries of layer  $Y$ .

Assume a homogeneous formation of elastic property  $\mathbf{p}_0$  where a layer (layer  $Y$ ) of thickness  $\Delta z_L$  and elastic property  $\mathbf{p}$  such that  $\mathbf{p} = \mathbf{p}_0 + \Delta \mathbf{p}$  is inserted. This assumption divides the medium in three regions: region  $I$  has elastic property  $\mathbf{p}_0$  and contains an incident and reflected wave with complex amplitudes  $A$  and  $B$ , respectively; region  $II$  has thickness  $\Delta z_L$  with elastic property  $\mathbf{p}$  and a transmitted and reflected waves with complex amplitudes  $C$  and  $D$ , respectively; and region  $III$  has elastic property  $\mathbf{p}_0$  and contains only a transmitted wave with complex amplitude  $E$ ;  $s_r = s^{\{l\}}(\mathbf{p}_0, f)$  and  $s_p = s^{\{l\}}(\mathbf{p}, f)$  are the slownesses of the homogeneous formations with elastic properties  $\mathbf{p}_0$  and  $\mathbf{p}$ , respectively. The upper and lower location of the boundaries of layer  $Y$  are  $z_u$  and  $z_l$ , respectively, as shown in Figure A-1.

Using Lamé's theorem (Aki and Richards, 2002), we express the displacement field  $u$  as  $u = \frac{\partial \phi}{\partial z}$ , where  $\phi$  is the scalar wave potential. Because  $u$  satisfies the wave equation,  $\phi$  satisfies the Helmholtz equation whose solution in regions  $I$ ,  $II$ , and  $III$  is given by

$$\phi_I(z) = Ae^{-ik_I z} + Be^{ik_I z}, \quad (\text{A-2})$$

$$\phi_{II}(z) = Ce^{-ik_{II} z} + De^{ik_{II} z}, \quad (\text{A-3})$$

$$\phi_{III}(z) = Ee^{-ik_{III} z}, \quad (\text{A-4})$$

where  $k_i$  is the wavenumber of layer  $i$ . In this example  $k_I = k_{III} = k_r$  and  $k_{II} = k_p$ . We assume that  $A$  (the incident amplitude) is known and calculate the four unknowns  $B$ ,  $C$ ,  $D$ , and  $E$  by applying continuity of the displacement  $u$  and stress  $\sigma$  at  $z_l$  and  $z_u$ ;  $u$  and  $\sigma$  are given by

$$u(z) = \frac{\partial \phi}{\partial z}, \quad (\text{A-5})$$

$$\sigma(z) = \lambda \frac{\partial u}{\partial z}, \quad (\text{A-6})$$

where  $\lambda = \rho c^2$ , with  $\rho$  and  $c$  being the density and velocity of the wave mode of the layer, respectively. We solve the system of equations

$$\begin{bmatrix} k_r e^{ik_r z_l} & k_p e^{-ik_p z_l} & -k_p e^{ik_p z_l} & 0 \\ -\lambda_r k_r^2 e^{ik_r z_l} & \lambda_p k_p^2 e^{-ik_p z_l} & \lambda_p k_p^2 e^{ik_p z_l} & 0 \\ 0 & -k_p e^{-ik_p z_u} & k_p e^{ik_p z_u} & k_r e^{-ik_r z_u} \\ 0 & -\lambda_p k_p^2 e^{-ik_p z_u} & -\lambda_p k_p^2 e^{ik_p z_u} & \lambda_r k_r^2 e^{-ik_r z_u} \end{bmatrix} \begin{bmatrix} B \\ C \\ D \\ E \end{bmatrix} = \begin{bmatrix} Ak_r e^{-ik_r z_l} \\ A\lambda_r k_r^2 e^{-ik_r z_l} \\ 0 \\ 0 \end{bmatrix}, \quad (\text{A-7})$$

to obtain

$$B = \frac{Ae^{-2ik_r z_l}(e^{2ik_p z_l} - e^{2ik_p z_u})(k_r^2 - k_p^2)}{e^{2ik_p z_l}(k_r - k_p)^2 - e^{2ik_p z_u}(k_r + k_p)^2}, \quad (\text{A-8})$$

$$C = \frac{iAe^{-i(k_r z_l - k_p z_u)} k_r (k_r + k_p)}{2ik_r k_p \cos[k_p(z_l - z_u)] + (k_r^2 + k_p^2) \sin[k_p(z_l - z_u)]} \quad (\text{A-9})$$

$$D = \frac{2Ae^{-i(k_r - k_p)z_l} k_r (k_r - k_p)}{e^{2ik_p z_l} (k_r - k_p)^2 - e^{2ik_p z_u} (k_r + k_p)^2} \quad (\text{A-10})$$

and

$$E = \frac{2iAe^{-ik(z_l - z_u)} k_r k_p}{2ik_r k_p \cos[k_r(z_l - z_u)] + (k_r^2 + k_p^2) \sin[k_p(z_l - z_u)]} \quad (\text{A-11})$$

Therefore, when layer  $Y$  is between receivers  $j$  and  $j + 1$ , the spectrum  $X_i$  at each receiver  $i$  can be written as

$$[X_1(f), \dots, X_j(f), X_{j+1}(f), X_{j+2}(f), \dots, X_N(f)] = [A, AZ + BZ^*, \dots, AZ^{(j-1)} + BZ^{*(j-1)}, Ce^{-ik_p j \Delta z_L} + De^{ik_p j \Delta z_L}, EZ^{(j+1)} \dots, EZ^{(N-1)}], \quad (\text{A-12})$$

where  $Z = e^{-ik_r \Delta z_L}$  and  $Z^*$  is the complex conjugate of  $Z$ .

Huang et al. (2015) ignore the reflections given by  $B$  and  $D$  because in the limits of perturbation theory  $|k_r - k_p|/k_r \ll 1$ , therefore  $|B| \ll |C|$  and  $|D| \ll |E|$ .

Another method to remove the interference caused by the reflections without imposing  $|B| = 0$  is to calculate the axial sensitivity functions using an anti-reflective layer by taking  $\Delta z_L = \frac{\pi n}{k_p}$ , where  $n$  is a positive integer (see equation A-8).

In Figures A-2 and A-3, we compare  $G^{\{l\}}/\Delta z_L$  to the product  $FS^{\{l\}}/\Delta z_L$  normalized by  $s^{\{l\}}(\mathbf{p}_0, f)/\mathbf{p}_0$  calculated for LWD and wireline tools, respectively, where  $\Delta z_L$  is the thickness of the layer used to construct the axial sensitivity functions. We observe that the sensitivities calculated using both methods agree within a relative difference of 1%. The advantages of calculating the axial sensitivity using the product  $FS$  are: (1) it is more efficient because it does

not require processing the spectrum (equation A-12) for every position  $z$ , and (2) it decouples the effects of tool geometry and intrinsic elastic properties of formations on the measured acoustic logs.

1  
2  
3  
4  
5  
6  
7  
8  
9  
10  
11  
12  
13  
14  
15  
16  
17  
18  
19  
20  
21  
22  
23  
24  
25  
26  
27  
28  
29  
30  
31  
32  
33  
34  
35  
36  
37  
38  
39  
40  
41  
42  
43  
44  
45  
46  
47  
48  
49  
50  
51  
52  
53  
54  
55  
56  
57  
58  
59  
60

## NOMENCLATURE

**List of symbols**

$\{c\}$ : compressional mode

$\{fl\}$ : flexural mode

$\{q\}$ : quadrupole mode

$\{st\}$ : Stoneley mode

$|A|, |B|, |C|, |D|, |E|$ : amplitudes of transmitted and reflected waves

$\alpha$ : regularization parameter

$c_{11}, c_{13}, c_{33}, c_{44}, c_{66}$ : stiffness coefficients

$\varepsilon, \delta, \gamma$ : Thomsen's parameters

$\phi$ : wave potential

$\rho$ : density

$c$ : velocity

$d$ : depth (of the log)

$s(z)$ : slowness at depth  $z$

$s_r$ : slowness of the reference homogeneous formation

$s_p$ : slowness of the perturbed homogeneous formation

$vp_v$ : vertical compressional velocity

$ss_v$ : vertical shear slowness

$f$ : frequency

$\mathbf{g}(\mathbf{p})$ : forward model of slownesses of a homogeneous formation with elastic property  $\mathbf{p}$

## Geophysics Interpretation of VTI Formations

31

$e_1$ : cost function of inversion *Step 1*

$e_2$ : cost function of inversion *Step 2*

$F$ : averaging function

$k_i$ : wavenumber of layer  $i$

$L$ : length of receiver array

$N$ : total number of receivers

$T$ : total travel time

$D_T$ : total distance

$\{l\}$ : borehole mode

$G^{\{l\}}$ : normalized axial sensitivity function of wave mode  $\{l\}$

$\mathbf{J}$ : Jacobian matrix

$\mathbf{m}$ : vector of model parameters

$S_k^{\{l\}}$ : sensitivity of mode  $\{l\}$  to stiffness coefficient  $c_k$

$s^{\{l\}}$ : slowness of mode  $\{l\}$

$\mathbf{s}_k$ : slowness vector of layer  $k$  at all frequencies

$\bar{s}^{\{l\}}(d, f)$ : average slowness of mode  $\{l\}$  at depth  $d$  and frequency  $f$

$\sigma$ : 1D-stress

$\mathbf{p}_0$ : vector of the elastic properties of the reference formation

$\mathbf{p}$ : vector of the elastic properties of a homogeneous formation

$\mathbf{d}_{\log}$ : data vector (slowness log)

$\mathbf{W}_n$ : regularization weighing matrix

$X_i$ : spectrum at receiver  $i$

$\Delta z_L$ : vertical thickness of perturbed layer

$\Delta z_R$ : vertical distance between two consecutive receivers

$\Delta s(f_i)$ : uncertainty in the estimated slowness  $s$  at frequency  $f_i$

$\Delta c_k$ : uncertainty in the estimated stiffness coefficient  $c_k$

$\Sigma$ : diagonal matrix whose component are  $\Sigma_{ii} = 1/\sigma_{s(f_i)}$

$\sigma_{s(f)}$ : standard deviation of the error of the estimated slowness at frequency  $f$

$\sigma_{c_k}$ : standard deviation of the error of the estimated stiffness coefficient  $c_k$

$z_l$ : lower boundary of layer  $Y$

$z_u$ : upper boundary of layer  $Y$

$u$ : 1D-displacement

### List of acronyms

1D: one dimensional

2DFD: two-dimensional finite difference

2DFE: two-dimensional finite element

CPU: central processing unit

LWD: logging while drilling

SNR: signal-to-noise ratio

TI: transverse isotropy

VTI: vertical transverse isotropy

## REFERENCES

- Aki, K. and P.G. Richards, 2002, Quantitative seismology, 2nd Edition: University Science Books.
- Aster, R., B. Borchers, and C. Thurber, 2005, Parameter estimation and inverse problems: Elsevier Academic.
- Berryman, J.G., V.Y. Grechka, and P.A. Berge, 1999, Analysis of Thomsen parameters for finely layered VTI media, *Geophysical Prospecting*, **47**, no. 6, pp. 959–978.
- Foti, S., L. Sambuelli, L. V. Socco, and C. Strobbia, 2002, Spatial sampling issues in fk analysis of surface waves: Symposium on the Application of Geophysics to Engineering and Environmental Problems 2002: Society of Exploration Geophysicists, p. SEI8-SEI8.
- Hsu, K., and S. K. Chang, 1987, Multiple-shot processing of array sonic waveforms for high resolution sonic logs: *Geophysics*, **52**, 1376–1390, doi: 10.1190/1.1442250.
- Huang, S., P.J. Matuszyk, and C. Torres-Verdín, 2015, Spatial sensitivity functions for rapid numerical simulation of borehole sonic measurements in vertical wells: *Geophysics*, **80**, no. 5, D459–D480.
- Huang, S. and C. Torres-Verdín, 2016, Inversion-based interpretation of borehole sonic measurements using semianalytical spatial sensitivity functions: *Geophysics*, **81**, no. 2, D111–D124.
- Maalouf and Torres-Verdín, 2017, Inversion-based method to mitigate noise in borehole sonic logs: *Geophysics*, **83**, no. 2, pp. D61–D71.

Matuszyk, P.J. and C., Torres-Verdín, 2014, Frequency-domain simulation of logging-while-drilling borehole sonic waveforms: *Geophysics*, **79**, no. 2, pp. D99–D113.

Murphy, E., S.R. Barraza, M. Gu, D. Gokaraju, M.E. Far, and J. Quirein, 2015, New models for acoustic anisotropic interpretation in shale: Presented at the SPWLA 56th Annual Logging Symposium, Long Beach, California, USA.

Peyret, A. and C. Torres-Verdín, 2006, Assessment of shoulder-bed, invasion, and lamination effects on borehole sonic log: A numerical sensitivity study: Presented at the SPWLA 47th Annual Logging Symposium, Veracruz, Mexico.

Scheibner, D., S. Yoneshima, Z. Zhang, W. Izuhara, Y. Wada, P. Wu, F. Pampuri, and M. Pelorosso, 2010, Slow formation shear from an LWD tool: Quadrupole inversion with a Gulf of Mexico example: Presented at the SPWLA 51st Annual Logging Symposium, Perth, Australia.

Sinha, B. K., A. N. Norris, and S. K. Chang, 1994, Borehole flexural modes in anisotropic formations: *Geophysics*, **59**, no. 7, 1037–1052.

Sinha, B. K., E. Simsek, and S. Asvadurov, 2009, Influence of a pipe tool on borehole modes: *Geophysics*, **74**, no. 3, E111–E123.

Sinha, B. K., A. Donald, J. Walsh, and T. Lei, 2014, Anisotropic elastic constants from dipole flexural dispersion in unconventional shale-gas reservoirs: 84th Annual International Meeting, SEG, Expanded Abstracts, 596–600, Denver, CO, USA.

Sinha, B. K., L. Xu, O. Magbagbeola, and K. Macphail, 2016, A new workflow for geomechanical analyses in the Marcellus Shale Gas Basin: 86th Annual International Meeting, SEG, Expanded Abstracts, 652–656, Dallas, Texas, USA.

Spikes, K. T., 2014, Error estimates of elastic components in stress-dependent VTI media: Journal of Applied Geophysics, **108**, p. 110–123, doi:10.1016/j.jappgeo.2014.06.015.

Su, Y.D., X.M. Tang, C.X. Zhuang, S. Xu, and L. Zhao, 2013, Mapping formation shear-velocity variation by inverting logging-while-drilling quadrupole-wave dispersion data: Geophysics, **78**, no. 6, D491–D498.

Tang, X. and A. Cheng, 2004, Quantitative borehole acoustic methods: Pergamon Press.

Thomsen, L., 1986, Weak elastic anisotropy: Geophysics, **51**, no. 10, 1954–1966.

Tutuncu, A.N., 2010, Anisotropy, compaction and dispersion characteristics of reservoir and seal shales: 44th US Rock Mechanics Symposium and 5th US-Canada Rock Mechanics Symposium, ARMA, 10–344, Salt Lake City, Utah, USA.

Vernik, L. and X. Liu, 1997, Velocity anisotropy in shales: A petrophysical study: Geophysics, **62**, no. 2, pp.521–532.

Walsh, J., B. Sinha, and A. Donald, 2006, Formation anisotropy parameters using borehole sonic data: Presented at the 47th SPWLA Annual Logging Symposium, Veracruz, Mexico.

Walsh, J., B. Sinha, T. Plona, D. Miller, D. Bentley, and M. Ammerman, 2007, Derivation of anisotropic parameters in a shale using borehole sonic data: 77th Annual International Meeting, SEG, Expanded Abstracts, 323–327, San Antonio, TX, USA.

Xu, Y., J. Hou, and C. Torres-Verdín, 2005, Fast and efficient 2.5D time-domain simulation of multi-pole sonic logs: elastic and poro-elastic transverse isotropic formulations: Presented at the Annual Meeting of UT Austin's Research Consortium on Formation Evaluation, Austin, TX, USA.

Yan, F., D.H. Han, S. Sil, and X.L. Chen, 2016, Analysis of seismic anisotropy parameters for sedimentary strata: *Geophysics*, **81**, no. 5, D495–D502.

## LIST OF FIGURES

**Figure A-1:** Homogeneous formation with an embedded horizontal layer (layer  $Y$ ) of perturbed elastic properties. Lower and upper boundaries of layer  $Y$  are  $z_l$  and  $z_u$ , respectively. The amplitudes of the transmitted waves are  $|A|$ ,  $|C|$ , and  $|E|$ , while the amplitudes of the reflected waves are  $|B|$  and  $|D|$ . .....**Error! Bookmark not defined.**

**Figure A-2:** Axial sensitivity of the quadrupole mode measured with an LWD instrument at 4 kHz, 5 kHz, 6 kHz, and 7 kHz to perturbations of stiffness coefficients. The axial sensitivity function  $G/\Delta zL$  calculated using equation A-1, is shown with circles, while the sensitivity function calculated using the product of  $FS/\Delta zL$  normalized by  $p_0/sl p_0, f$  is shown with continuous lines.....**Error! Bookmark not defined.**

**Figure A-3:** Axial sensitivity of the flexural mode measured with a wireline tool at 3 kHz, 4 kHz, 5 kHz, 6 kHz, and 7 kHz to perturbations of stiffness coefficients. The axial sensitivity function  $G/\Delta zL$ , calculated using equation A-1, is shown with circles, while the sensitivity function calculated using the product of  $FS/\Delta zL$  normalized by  $p_0/sl p_0, f$  is shown with continuous lines.....**Error! Bookmark not defined.**

**Figure 1:** Normalized frequency-dependent sensitivity of the quadrupole mode to  $c_{11}$ ,  $c_{13}$ ,  $c_{33}$ ,  $c_{44}$ , and  $c_{66}$ , for the (a) slow and (b) fast formations logged with an LWD instrument. ....**Error! Bookmark not defined.**

**Figure 2:** Normalized frequency-dependent sensitivity of the flexural mode to  $c_{11}$ ,  $c_{13}$ ,  $c_{33}$ ,  $c_{44}$ , and  $c_{66}$ , for the (a) slow and (b) fast formations logged with a wireline instrument....**Error! Bookmark not defined.**

**Figure 3:** Geometry and relative locations of the receivers (circles) of the acoustic instrument shown in grey. Total number of receivers is  $N$ . The mid-position between receivers  $i$  and  $i + 1$  is  $z_i$ ;  $d$  is the position of the center of the receiver array, and  $L$  is the length of the receiver array;  $\Delta zR$  is the distance between two consecutive receivers. The averaging function  $F$  is illustrated with crosses. ....**Error! Bookmark not defined.**

**Figure 4:** Values of the function  $F$  (equation 12) quantifying the spatial averaging introduced by sonic tools on slownesses measured with the (a) LWD and (b) wireline instruments given in Table 2. Circles represent the ratio of  $F$  by the inter-receiver distance,  $\Delta z$ . .....**Error! Bookmark not defined.**

**Figure 5:** (a) Comparison of quadrupole, compressional, and Stoneley slownesses of a homogeneous formation (black) to slownesses (red) estimated with the inversion-based interpretation method (*Step 2*). Slownesses used to initialize the inversion are shown in blue. (b) Actual, initial, and inverted stiffness coefficients are shown in black, blue, and red, respectively. The error,  $e$ , between actual and inverted coefficients varies between 0.03 GPa and 1.14 GPa. ....**Error! Bookmark not defined.**

**Figure 6:** Comparison of input logs (black continuous lines) to modeled logs (blue circles) of the (a) compressional, (b) Stoneley at 1 kHz, and (c) quadrupole modes at 4 kHz, 5 kHz, 6 kHz, and 7 kHz (from right to left) for the VTI formation of Example 2 logged with an LWD instrument. Black dashed lines identify the actual slownesses of layers while blue dashed lines identify the slownesses obtained from *Step 1* of the inversion method. Error bars superimposed to the inverted slownesses represent the 95% confidence interval. ....**Error! Bookmark not defined.**

**Figure 7:** Comparison of actual rock stiffness coefficients (black) to inverted coefficients obtained with the inversion (*Step 2*) (blue) method applied to slowness data mitigated for spatial averaging effects (Figure 6). Error bars superimposed to the inverted stiffness coefficients represent the 95% confidence interval.....**Error! Bookmark not defined.**

**Figure 8:** Comparison of input logs (black continuous lines) to modeled logs (blue circles) of the (a) compressional, (b) Stoneley at 1.5 kHz, and (c) quadrupole modes at 4.5 kHz, 5 kHz, 6 kHz, and 7 kHz (from right to left) for the VTI formation of Example 3 logged with an LWD instrument. Black dashed lines identify the actual slownesses of layers while blue dashed lines identify the slownesses obtained from *Step 1* of the inversion method. Error bars superimposed to the inverted slownesses represent the 95% confidence interval..... **Error! Bookmark not defined.**

**Figure 9:** Comparison of actual rock stiffness coefficients (black) to inverted coefficients obtained from the inversion (*Step 2*) (blue) method applied to slowness data mitigated for spatial averaging effects (Figure 8). Error bars superimposed to the inverted stiffness coefficients represent the 95% confidence interval.....**Error! Bookmark not defined.**

**Figure 10:** Comparison of actual rock stiffness coefficients (black) to inverted coefficients from the sequential (blue) and simultaneous (green) inversion. Red circles indicate the inverted slownesses obtained from the actual (averaged) logs. ....**Error! Bookmark not defined.**

**Figure 11:** Comparison of input logs (black continuous lines) to modeled logs (blue circles) of the (a) compressional, (b) Stoneley at 1 kHz, and (c) flexural modes at 3 kHz, 4 kHz, 5 kHz, 6 kHz, and 7 kHz (from right to left) for the VTI formation logged with a wireline tool. Black dashed lines identify the actual slownesses of layers while blue dashed lines identify the slownesses obtained from *Step 1* of the inversion method. Error bars superimposed to the inverted slownesses represent the 95% confidence interval. ....**Error! Bookmark not defined.**

**Figure 12:** (a) Flexural logs at 3 kHz to 7 kHz measured with a wireline tool in the VTI formation (continuous lines) and modeled assuming that the formation is isotropic (circles). The actual vertical shear slownesses of layers are shown with a black dashed line. (b) Data residuals between input (continuous lines) and modeled flexural logs (circles)...... **Error! Bookmark not defined.**

**Figure 13:** (a) Flexural logs at 3 kHz to 7 kHz measured with a wireline tool in the VTI formation (continuous lines) and modeled assuming that the formation is VTI (circles). The actual vertical shear slownesses of layers are shown with a black dashed line. (b) Data residuals between input (continuous lines) and modeled flexural logs (circles)...... **Error! Bookmark not defined.**

**Figure 14:** Comparison of actual rock stiffness coefficients (black) to coefficients obtained by applying the inversion (*Step 2*) (blue) method on the slowness data mitigated for spatial averaging effects (Figure 11). Error bars superimposed to the inverted stiffness coefficients represent the 95% confidence interval.....**Error! Bookmark not defined.**

**Figure 15:** (a) Comparison of quadrupole logs of the formation of Example 2 to the actual (black) and estimated (red) shear slownesses of layers. (b) Comparison of quadrupole logs of the formation of Example 3 to the actual (black) and estimated (red) shear slownesses of layers. ....**Error! Bookmark not defined.**

1  
2  
3  
4  
5  
6  
7  
8  
9  
10  
11  
12  
13  
14  
15  
16  
17  
18  
19  
20  
21  
22  
23  
24  
25  
26  
27  
28  
29  
30  
31  
32  
33  
34  
35  
36  
37  
38  
39  
40  
41  
42  
43  
44  
45  
46  
47  
48  
49  
50  
51  
52  
53  
54  
55  
56  
57  
58  
59  
60

LIST OF TABLES

**Table 1:** Summary of the assumed elastic properties for borehole fluid and rock formations. ....**Error! Bookmark not defined.**

**Table 2:** Geometric properties assumed for the LWD and wireline instruments. ....**Error! Bookmark not defined.**

**Table 3:** Description of *Step 2* of the inversion method. ....**Error! Bookmark not defined.**

**Table 4:** Parameters used during inversion in the synthetic examples examined in this paper. ....**Error! Bookmark not defined.**

**Table 5:** Relative bias and standard deviation of the error for the estimated stiffness coefficients in the synthetic examples examined in this paper. ....**Error! Bookmark not defined.**

**Table 6:** Ratio of relative error (norm). Stiffness coefficients are estimated with simultaneous and sequential inversions when calculating the ratio of relative error. .... **Error! Bookmark not defined.**

**Table 7:** Ratio of relative error (norm). Stiffness coefficients are estimated without and with de-averaging of well logs when calculating the ratio of relative error. .... **Error! Bookmark not defined.**

1  
2  
3  
4  
5  
6  
7  
8  
9  
10  
11  
12  
13  
14  
15  
16  
17  
18  
19  
20  
21  
22  
23  
24  
25  
26  
27  
28  
29  
30  
31  
32  
33  
34  
35  
36  
37  
38  
39  
40  
41  
42  
43  
44  
45  
46  
47  
48  
49  
50  
51  
52  
53  
54  
55  
56  
57  
58  
59  
60

**Table 1:** Summary of the assumed elastic properties for borehole fluid and rock formations.

	<b>Borehole</b>	<b>Slow Formation</b>	<b>Fast Formation</b>
$\rho$ (kg/m <sup>3</sup> )	1000	2500	2500
$c_{11}$ (GPa)	2.25	23.04	43.56
$c_{13}$ (GPa)	2.25	5.95	9.76
$c_{33}$ (GPa)	2.25	14.40	27.22
$c_{44}$ (GPa)	0	4.90	10.0
$c_{66}$ (GPa)	0	6.86	14.0

1  
2  
3  
4  
5  
6  
7  
8  
9  
10  
11  
12  
13  
14  
15  
16  
17  
18  
19  
20  
21  
22  
23  
24  
25  
26  
27  
28  
29  
30  
31  
32  
33  
34  
35  
36  
37  
38  
39  
40  
41  
42  
43  
44  
45  
46  
47  
48  
49  
50  
51  
52  
53  
54  
55  
56  
57  
58  
59  
60

**Table 2:** Geometric properties assumed for the LWD and wireline instruments.

	<b>LWD</b>	<b>Wireline</b>
<b>Number of receivers</b>	12	8
<b>Inter-receiver spacing (m)</b>	0.1017	0.1524
<b>Inner/outer radius (m)</b>	0.0254/0.0857	NA/0.046

**Table 3:** Description of *Step 2* of the inversion method.

Step	Coefficient to Estimate	Method	Data	Initial Guess of Coefficients $c_{ijinitial}$	Estimated Coefficient $c_{ijfinal}$
1	$c_{33}$	$c_{33} = v_{pv}^2 \rho$	Compressional log	N/A	$c_{33final}$
2	$c_{66}$	Minimize equation 17 using Levenberg-Marquardt	Stoneley log at low frequency	$c_{33initial} = c_{33final}$ , $c_{11initial} = c_{33final}$ , $c_{44initial} = \text{quadrupole/flexural log at low frequency}$ , $c_{66initial} = c_{44initial}$ , $c_{13initial} = c_{33final} - 2c_{44initial}$ .	$c_{66final}$
3	$c_{44}$	Minimize equation 17 using Levenberg-Marquardt	Quadrupole/ Flexural logs at low frequencies	$c_{33initial} = c_{33final}$ , $c_{66initial} = c_{66final}$ , $c_{44initial} = \text{quadrupole/flexural log at low frequency}$ , $c_{11initial} = (2\varepsilon + 1)c_{33final}$ , $\varepsilon = \gamma = \frac{c_{66final} - c_{44initial}}{2c_{44initial}}$ , $c_{13initial} = c_{33final} - 2c_{44initial}$ ,	$c_{44final}$
4	$c_{11}$ and $c_{13}$	Minimize equation 17 using Levenberg-Marquardt	Quadrupole/ Flexural logs at high frequencies	$c_{33initial} = c_{33final}$ , $c_{66initial} = c_{66final}$ , $c_{44initial} = c_{44final}$ , $c_{11initial} = (2\varepsilon + 1)c_{33final}$ , $\varepsilon = \gamma = \frac{c_{66final} - c_{44final}}{2c_{44final}}$ , $c_{13initial} = c_{33final} - 2c_{44final}$ ,	$c_{11final}$ and $c_{13final}$

**Table 4:** Parameters used during inversion in the synthetic examples examined in this paper.

	Tool type	Formation type	Frequency of Stoneley log used to estimate $c_{66}$	Frequency of quadrupole/flexural log used to estimate $c_{44}$	Frequencies of quadrupole/flexural logs used to estimate $c_{11}$ and $c_{13}$	Number of logging points
<b>Example 1</b>	LWD	Intermediate	1 kHz	3.5 kHz	4.5 kHz to 7 kHz	N/A
<b>Example 2</b>	LWD	Intermediate	1 kHz	3.5 kHz	4.5 kHz to 7 kHz	21
<b>Example 3</b>	LWD	Fast	1.5 kHz	4.5 kHz	4.5 kHz to 7 kHz	69
<b>Example 4</b>	Wireline	Intermediate	1 kHz	3 kHz	4.5 kHz to 7 kHz	21

**Table 5:** Relative bias and standard deviation of the error for the estimated stiffness coefficients in the synthetic examples examined in this paper.

	Maximum relative bias for the estimated $c_{33}$ , $c_{44}$ , and $c_{66}$	Maximum relative bias for the estimated $c_{11}$ and $c_{13}$	Maximum standard deviation of the error of estimated stiffness coefficients: $\sigma_{c_k}$
<b>Example 2</b>	1.6%	15.9%	1.43GPa
<b>Example 3</b>	6.75%	17.3%	3.86 GPa
<b>Example 4</b>	1.0%	16.2%	4.11 GPa

**Table 6:** Ratio of relative error (norm). Stiffness coefficients are estimated with simultaneous and sequential inversions when calculating the ratio of relative error.

	Ratio of relative error of estimated $c_{11}$ and $c_{13}$	
	$c_{11}$	$c_{13}$
<b>Layer 1</b>	0.96	1.11
<b>Layer 2</b>	3.87	2.87
<b>Layer 3</b>	1.25	0.70
<b>Layer 4</b>	1.86	2.60
<b>Layer 5</b>	3.00	> 100
<b>Layer 6</b>	1.29	1.83
<b>Layer 7</b>	1.82	1.32
<b>Layer 8</b>	0.95	1.06
<b>Layer 9</b>	2.55	4.75
<b>Layer 10</b>	1.42	2.74
<b>Layer 11</b>	0.10	0.25

**Table 7:** Ratio of relative error (norm). Stiffness coefficients are estimated without and with de-averaging of well logs when calculating the ratio of relative error.

	Ratio of relative error of estimated $c_{ij}$				
	$c_{11}$	$c_{13}$	$c_{33}$	$c_{44}$	$c_{66}$
<b>Layer 1</b>	0.04	1.54	1.29	1.06	7.39
<b>Layer 2</b>	0.96	1.90	11.45	3.20	0.59
<b>Layer 3</b>	0.47	1.12	9.37	3.73	2.74
<b>Layer 4</b>	0.74	1.12	43.27	1.51	30.19
<b>Layer 5</b>	0.31	> 100	9.91	2.64	14.21
<b>Layer 6</b>	0.47	1.53	8.22	0.63	66.08
<b>Layer 7</b>	0.09	0.95	4.88	4.39	0.57
<b>Layer 8</b>	2.94	1.46	9.15	2.04	7.82
<b>Layer 9</b>	2.29	0.77	2.73	0.97	1.03
<b>Layer 10</b>	0.34	2.35	38.53	0.70	22.29
<b>Layer 11</b>	0.69	0.56	10.97	1.98	0.77

1  
2  
3  
4  
5  
6  
7  
8  
9  
10  
11  
12  
13  
14  
15  
16  
17  
18  
19  
20  
21  
22  
23  
24  
25  
26  
27  
28  
29  
30  
31  
32  
33  
34  
35  
36  
37  
38  
39  
40  
41  
42  
43  
44  
45  
46  
47  
48  
49  
50  
51  
52  
53  
54  
55  
56  
57  
58  
59  
60

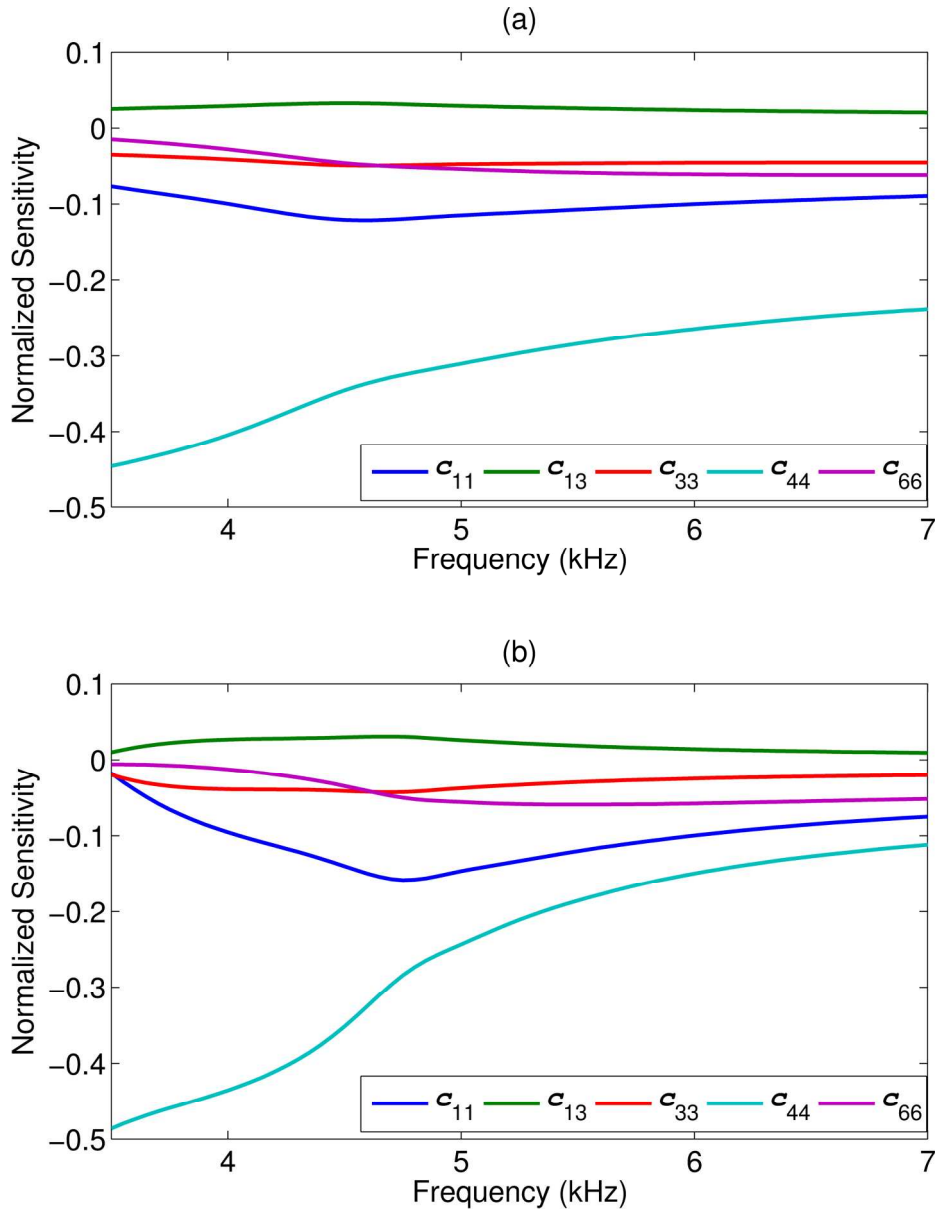


Figure 1

178x231mm (300 x 300 DPI)

1  
2  
3  
4  
5  
6  
7  
8  
9  
10  
11  
12  
13  
14  
15  
16  
17  
18  
19  
20  
21  
22  
23  
24  
25  
26  
27  
28  
29  
30  
31  
32  
33  
34  
35  
36  
37  
38  
39  
40  
41  
42  
43  
44  
45  
46  
47  
48  
49  
50  
51  
52  
53  
54  
55  
56  
57  
58  
59  
60

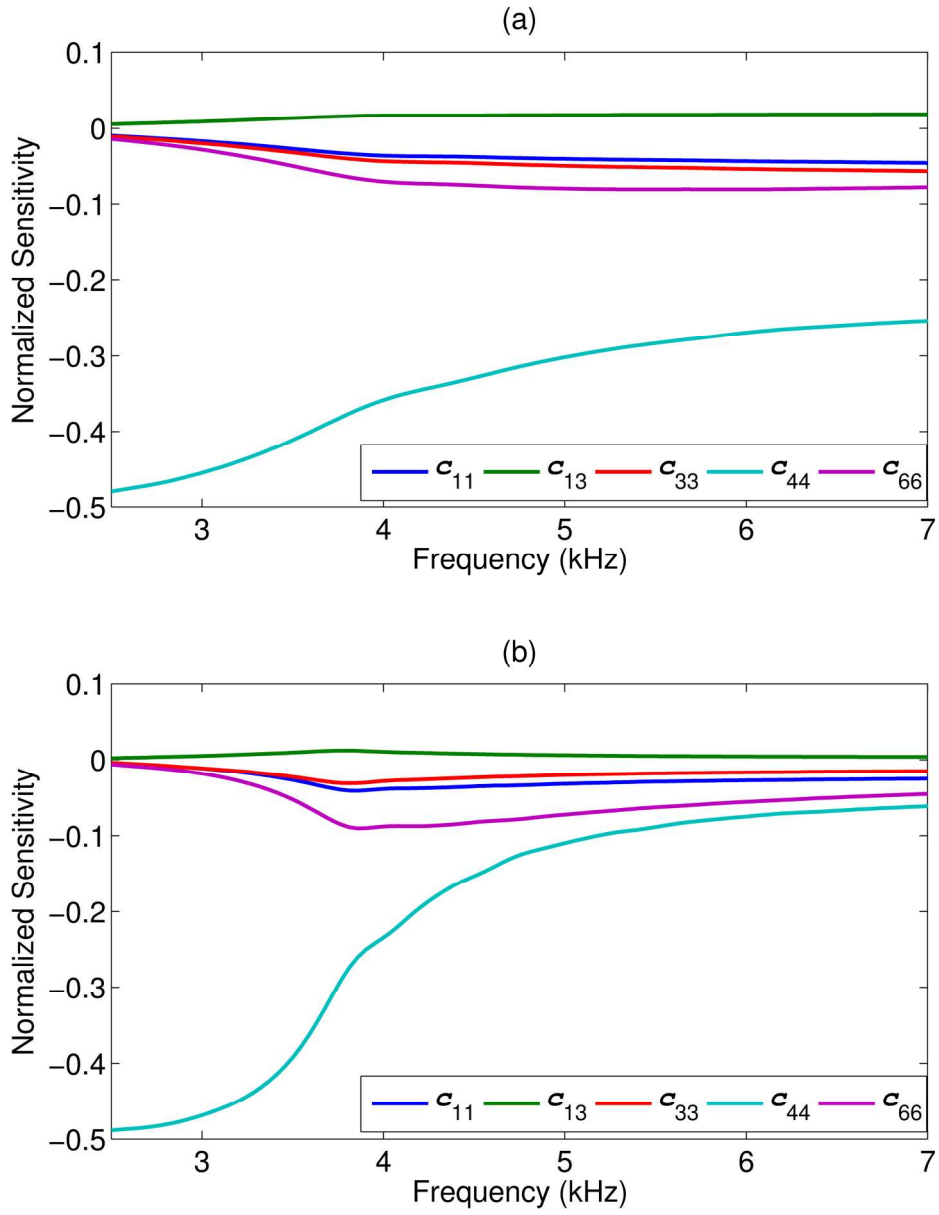


Figure 2

178x231mm (300 x 300 DPI)

1  
2  
3  
4  
5  
6  
7  
8  
9  
10  
11  
12  
13  
14  
15  
16  
17  
18  
19  
20  
21  
22  
23  
24  
25  
26  
27  
28  
29  
30  
31  
32  
33  
34  
35  
36  
37  
38  
39  
40  
41  
42  
43  
44  
45  
46  
47  
48  
49  
50  
51  
52  
53  
54  
55  
56  
57  
58  
59  
60

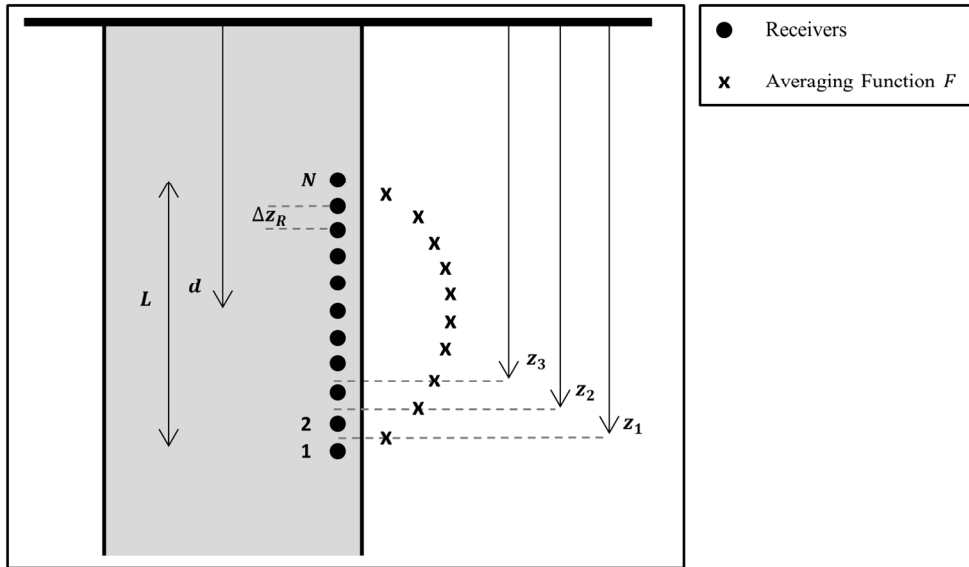


Figure 3

131x78mm (300 x 300 DPI)

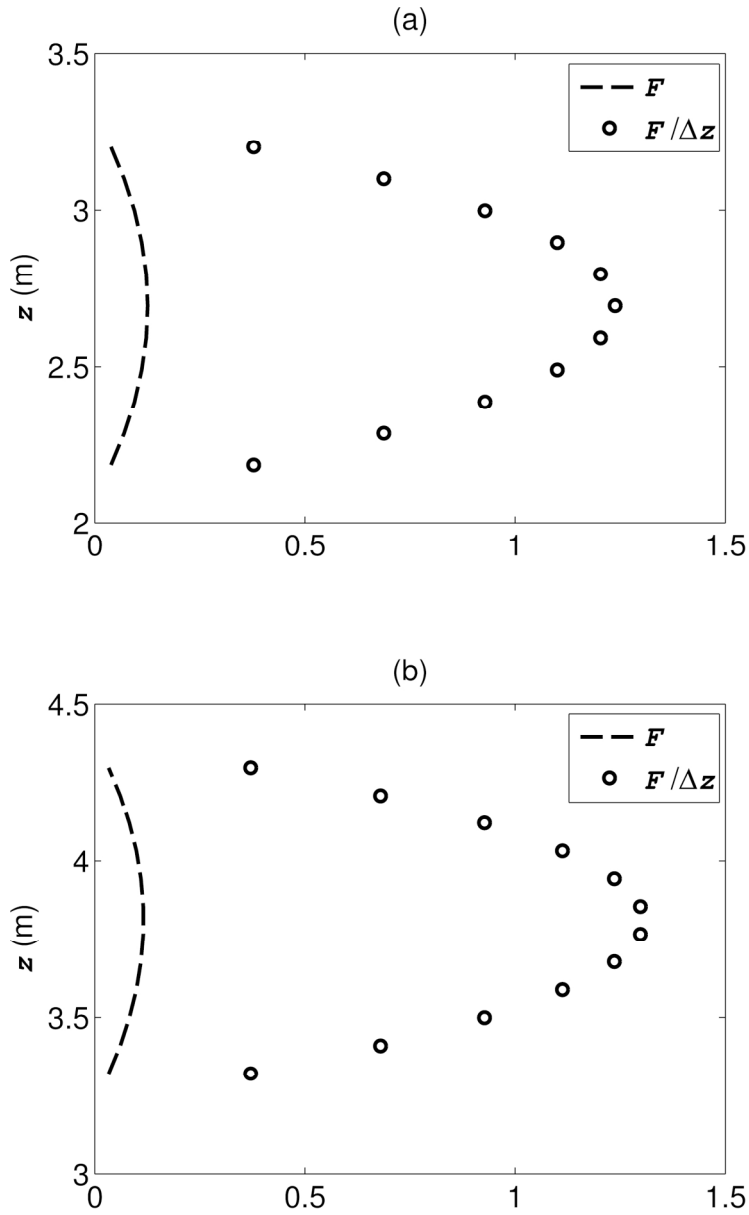


Figure 4

137x224mm (300 x 300 DPI)

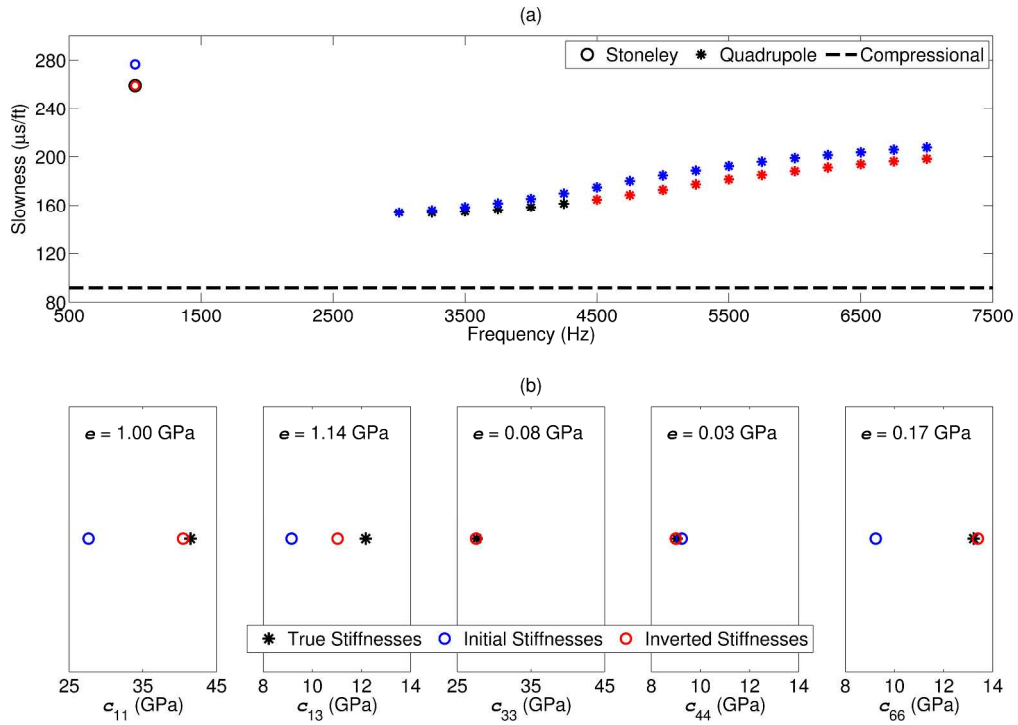


Figure 5

341x243mm (300 x 300 DPI)

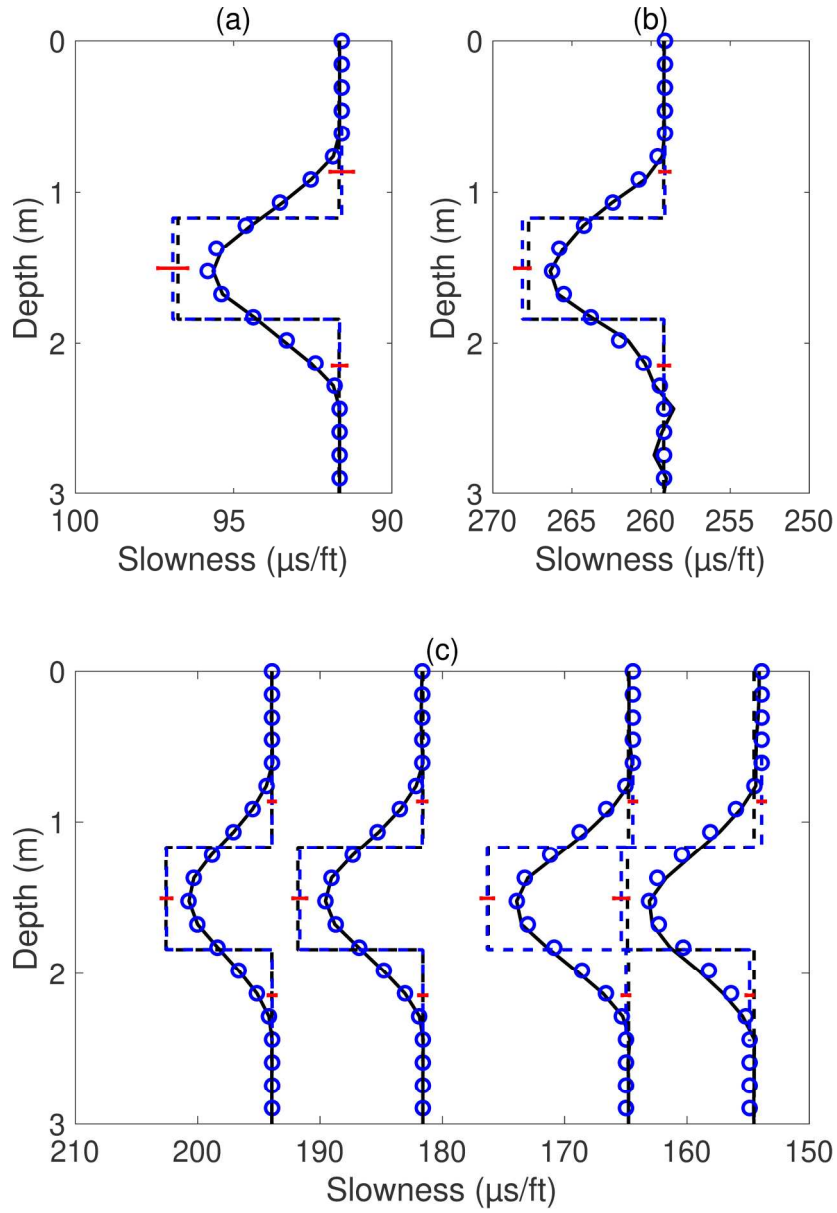


Figure 6

176x257mm (300 x 300 DPI)

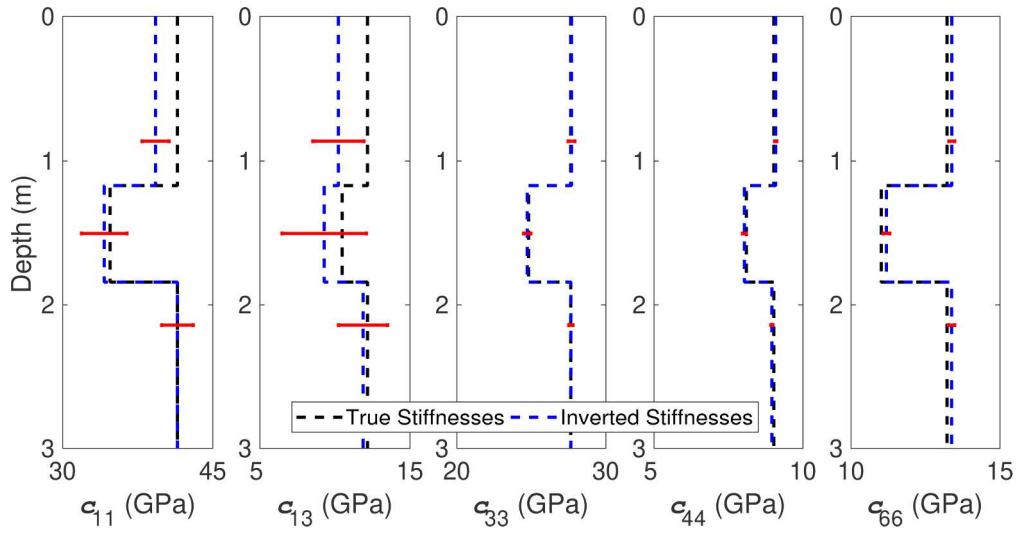


Figure 7

231x120mm (300 x 300 DPI)

1  
2  
3  
4  
5  
6  
7  
8  
9  
10  
11  
12  
13  
14  
15  
16  
17  
18  
19  
20  
21  
22  
23  
24  
25  
26  
27  
28  
29  
30  
31  
32  
33  
34  
35  
36  
37  
38  
39  
40  
41  
42  
43  
44  
45  
46  
47  
48  
49  
50  
51  
52  
53  
54  
55  
56  
57  
58  
59  
60

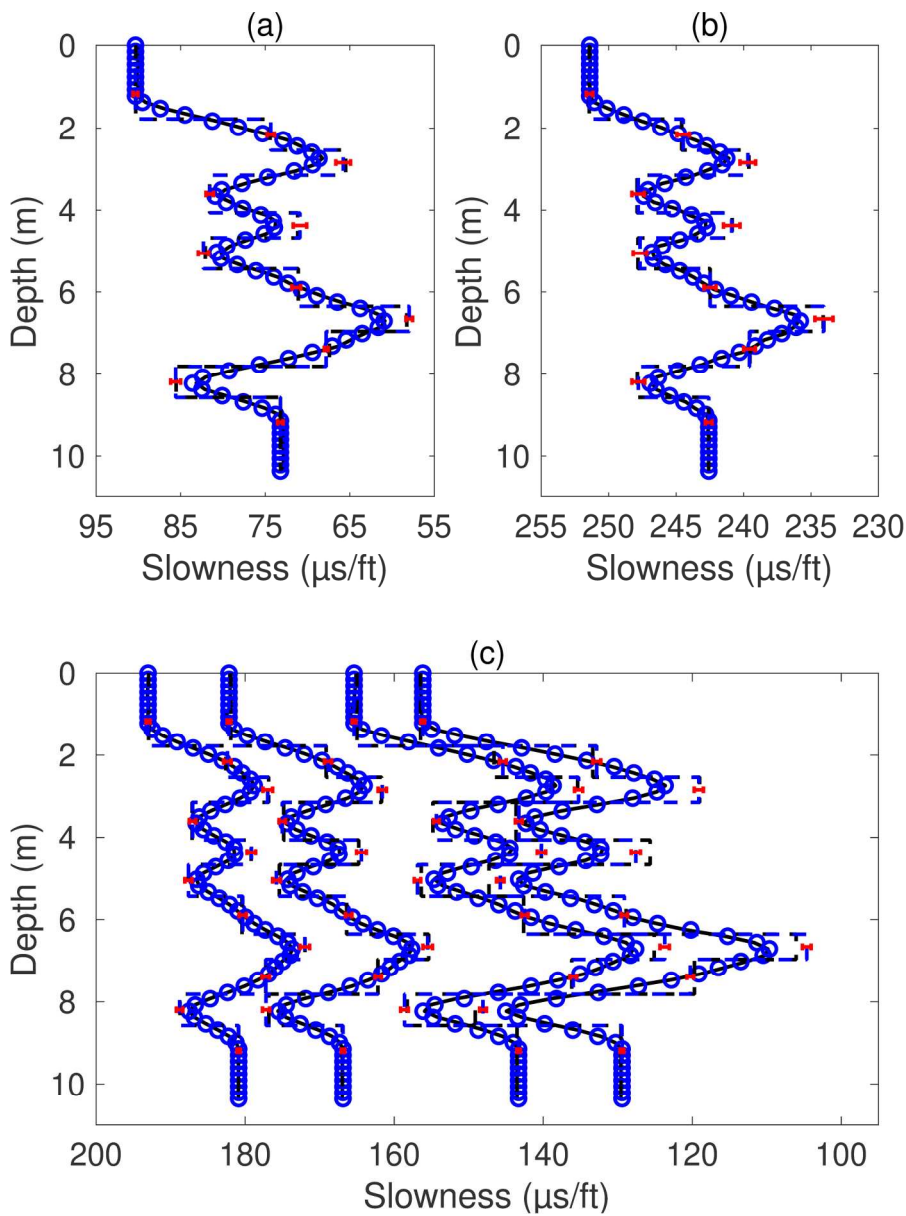


Figure 8

179x241mm (300 x 300 DPI)

1  
2  
3  
4  
5  
6  
7  
8  
9  
10  
11  
12  
13  
14  
15  
16  
17  
18  
19  
20  
21  
22  
23  
24  
25  
26  
27  
28  
29  
30  
31  
32  
33  
34  
35  
36  
37  
38  
39  
40  
41  
42  
43  
44  
45  
46  
47  
48  
49  
50  
51  
52  
53  
54  
55  
56  
57  
58  
59  
60

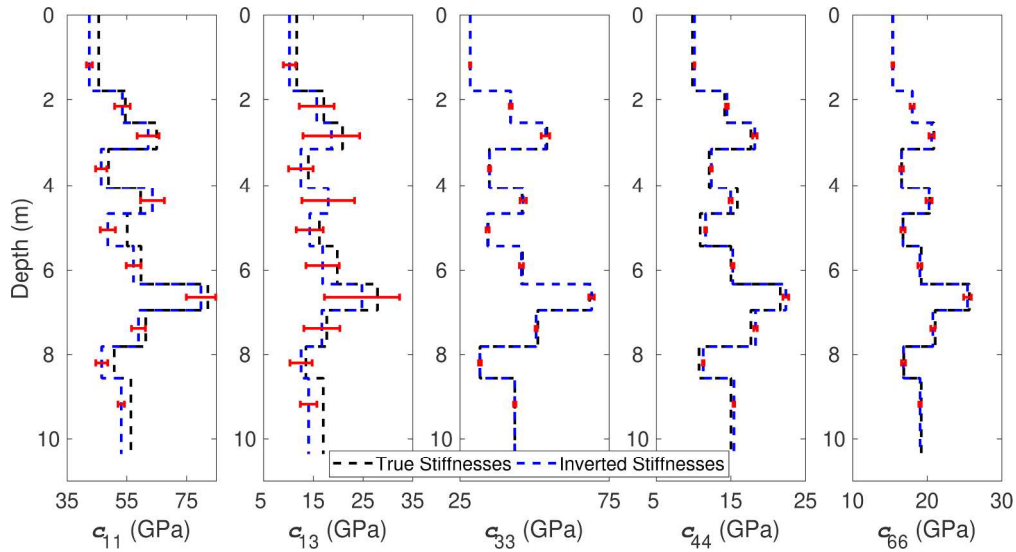


Figure 9

269x145mm (300 x 300 DPI)

1  
2  
3  
4  
5  
6  
7  
8  
9  
10  
11  
12  
13  
14  
15  
16  
17  
18  
19  
20  
21  
22  
23  
24  
25  
26  
27  
28  
29  
30  
31  
32  
33  
34  
35  
36  
37  
38  
39  
40  
41  
42  
43  
44  
45  
46  
47  
48  
49  
50  
51  
52  
53  
54  
55  
56  
57  
58  
59  
60

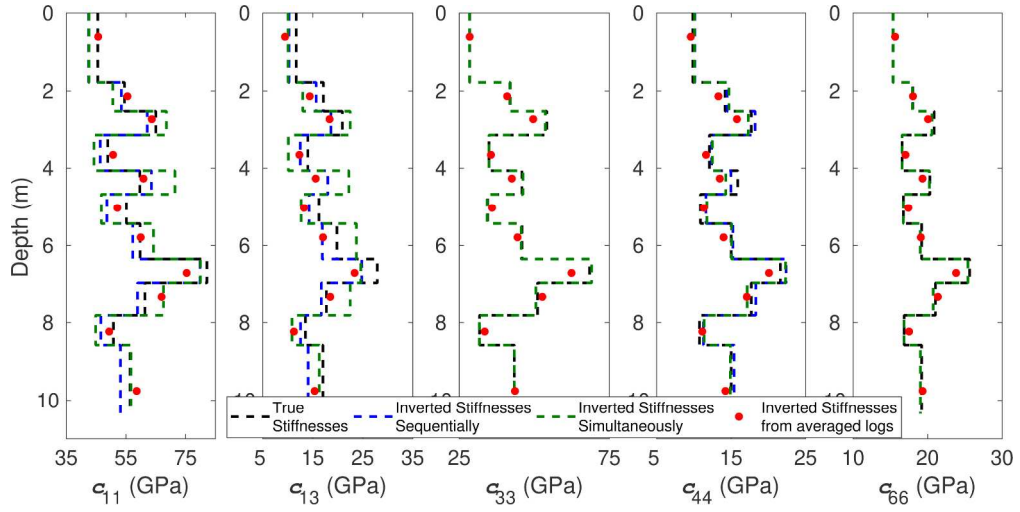


Figure 10

273x136mm (300 x 300 DPI)

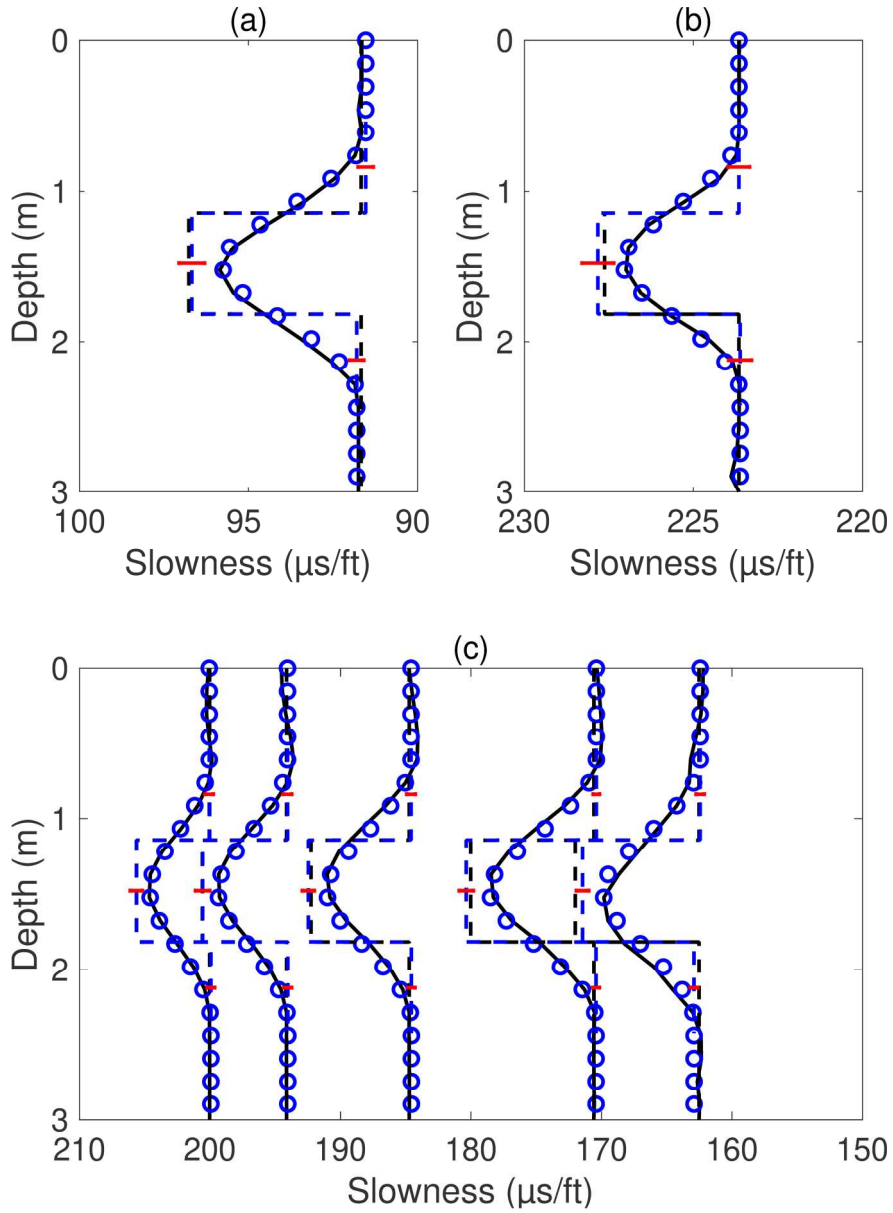


Figure 11

176x241mm (300 x 300 DPI)

1  
2  
3  
4  
5  
6  
7  
8  
9  
10  
11  
12  
13  
14  
15  
16  
17  
18  
19  
20  
21  
22  
23  
24  
25  
26  
27  
28  
29  
30  
31  
32  
33  
34  
35  
36  
37  
38  
39  
40  
41  
42  
43  
44  
45  
46  
47  
48  
49  
50  
51  
52  
53  
54  
55  
56  
57  
58  
59  
60

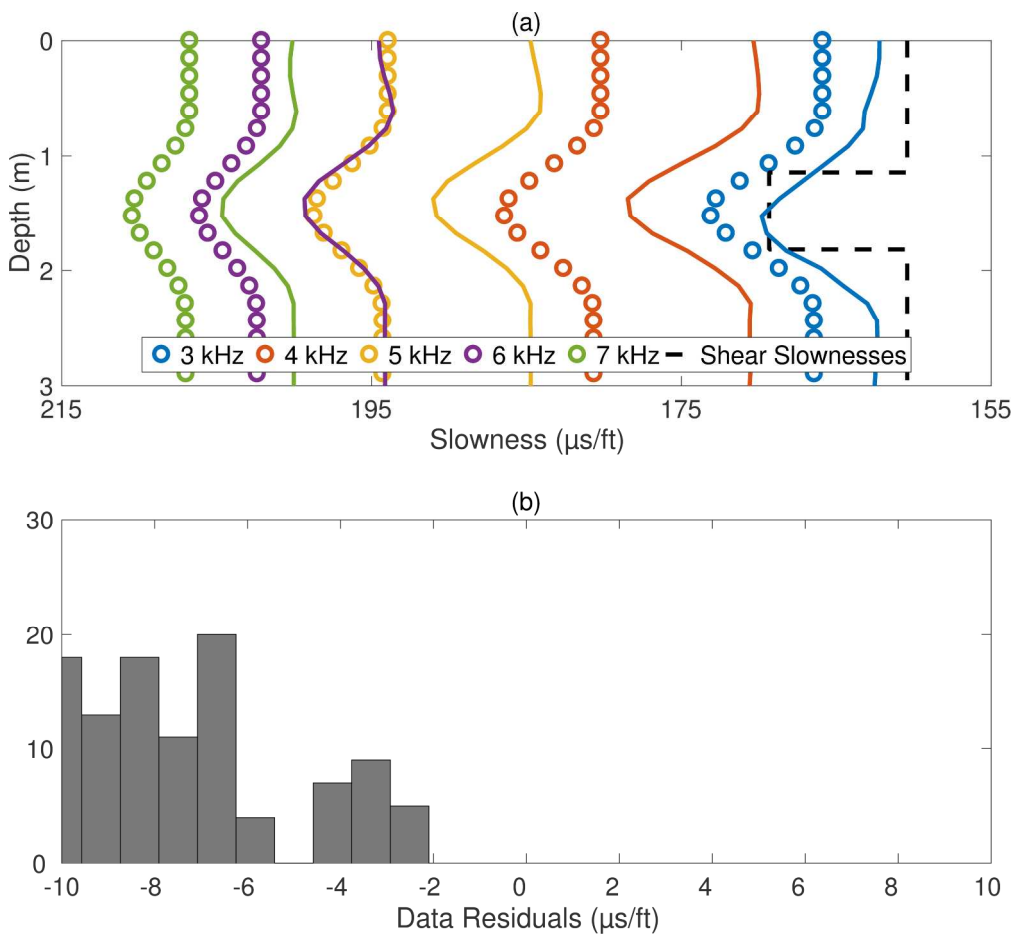


Figure 12

254x234mm (300 x 300 DPI)

1  
2  
3  
4  
5  
6  
7  
8  
9  
10  
11  
12  
13  
14  
15  
16  
17  
18  
19  
20  
21  
22  
23  
24  
25  
26  
27  
28  
29  
30  
31  
32  
33  
34  
35  
36  
37  
38  
39  
40  
41  
42  
43  
44  
45  
46  
47  
48  
49  
50  
51  
52  
53  
54  
55  
56  
57  
58  
59  
60

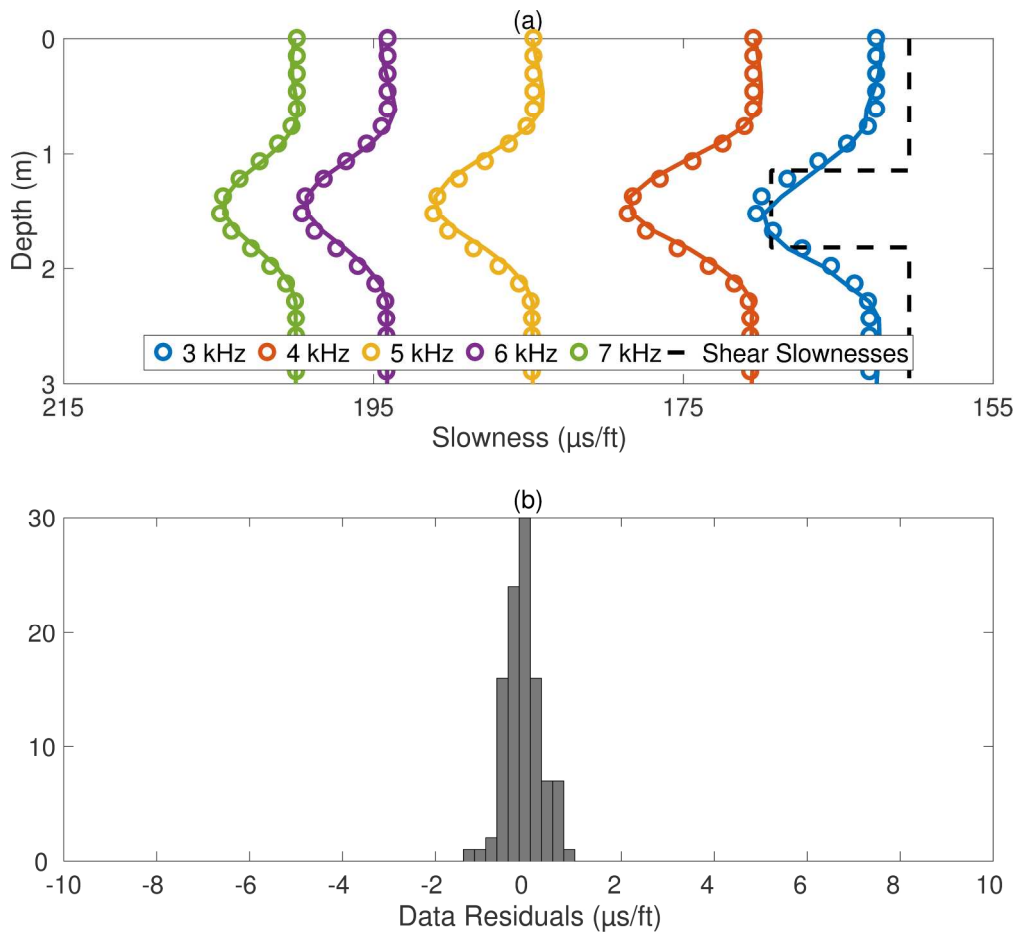


Figure 13

254x234mm (300 x 300 DPI)

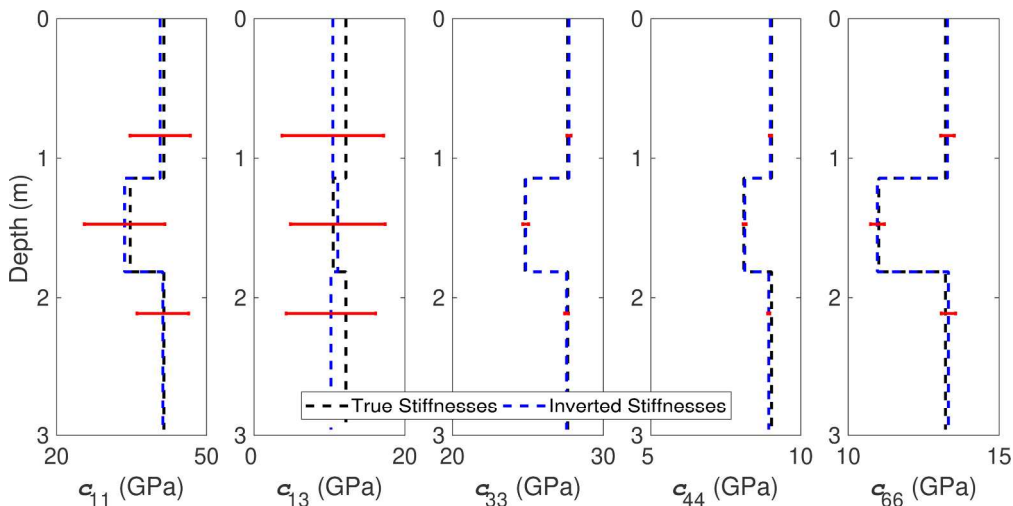


Figure 14

251x124mm (300 x 300 DPI)

1  
2  
3  
4  
5  
6  
7  
8  
9  
10  
11  
12  
13  
14  
15  
16  
17  
18  
19  
20  
21  
22  
23  
24  
25  
26  
27  
28  
29  
30  
31  
32  
33  
34  
35  
36  
37  
38  
39  
40  
41  
42  
43  
44  
45  
46  
47  
48  
49  
50  
51  
52  
53  
54  
55  
56  
57  
58  
59  
60

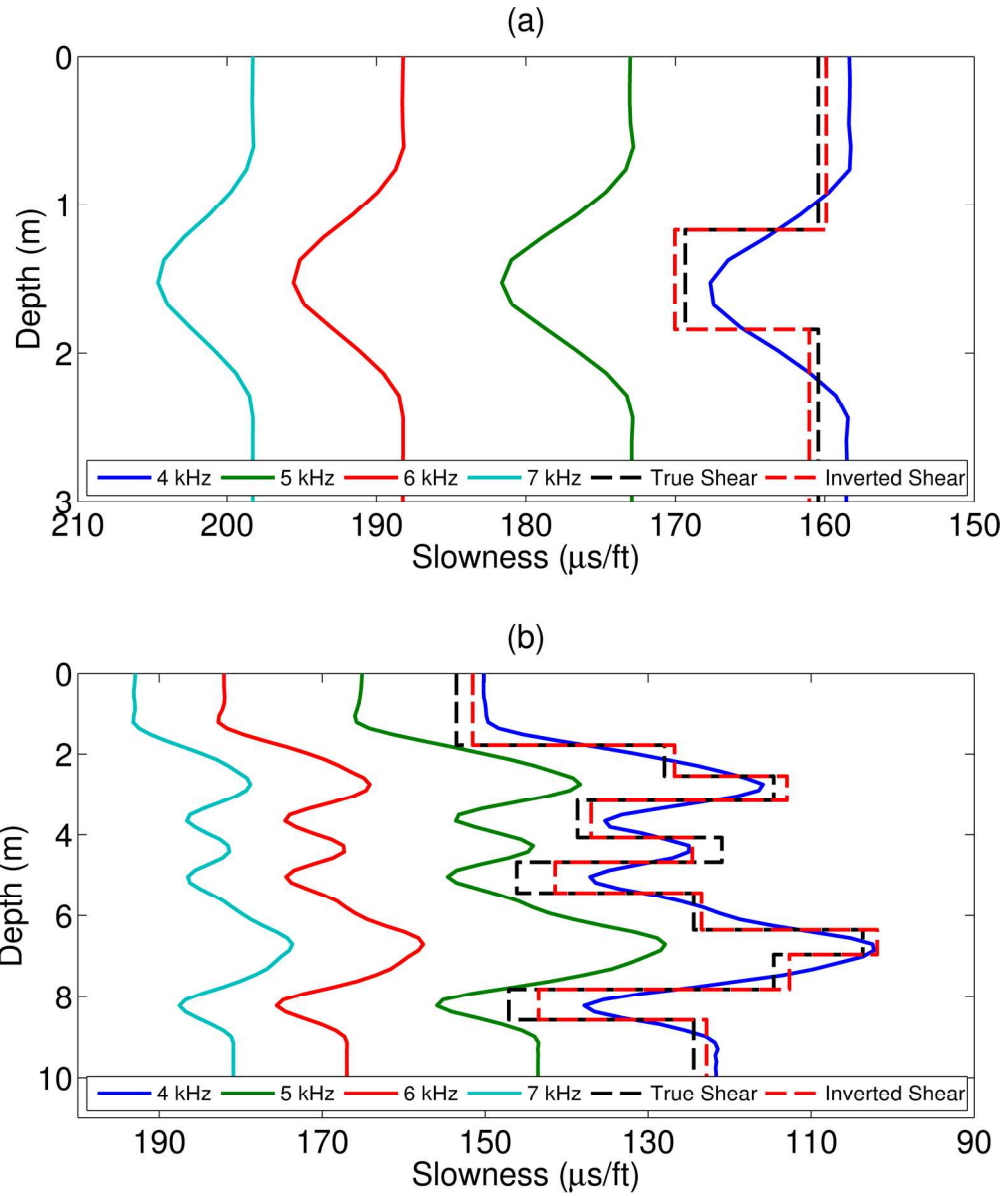


Figure 15

197x234mm (300 x 300 DPI)

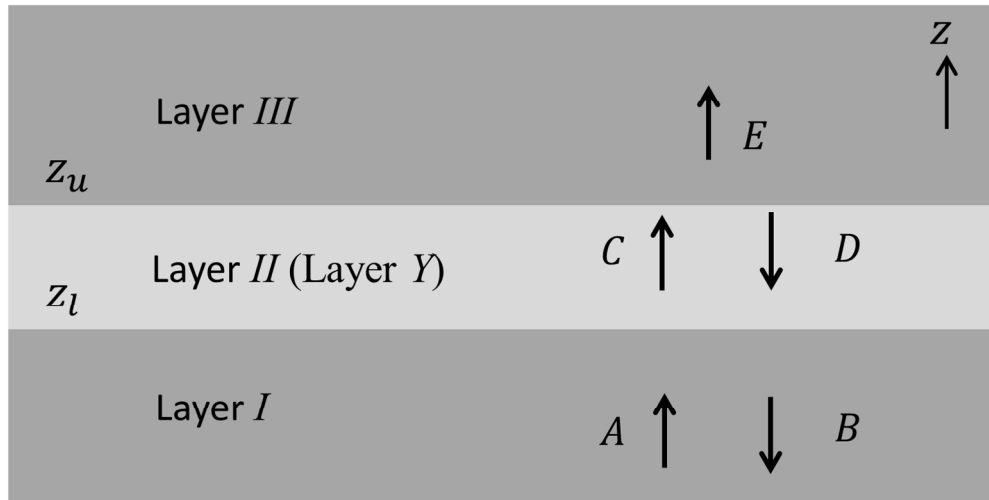


Figure A1

136x69mm (300 x 300 DPI)

1  
2  
3  
4  
5  
6  
7  
8  
9  
10  
11  
12  
13  
14  
15  
16  
17  
18  
19  
20  
21  
22  
23  
24  
25  
26  
27  
28  
29  
30  
31  
32  
33  
34  
35  
36  
37  
38  
39  
40  
41  
42  
43  
44  
45  
46  
47  
48  
49  
50  
51  
52  
53  
54  
55  
56  
57  
58  
59  
60

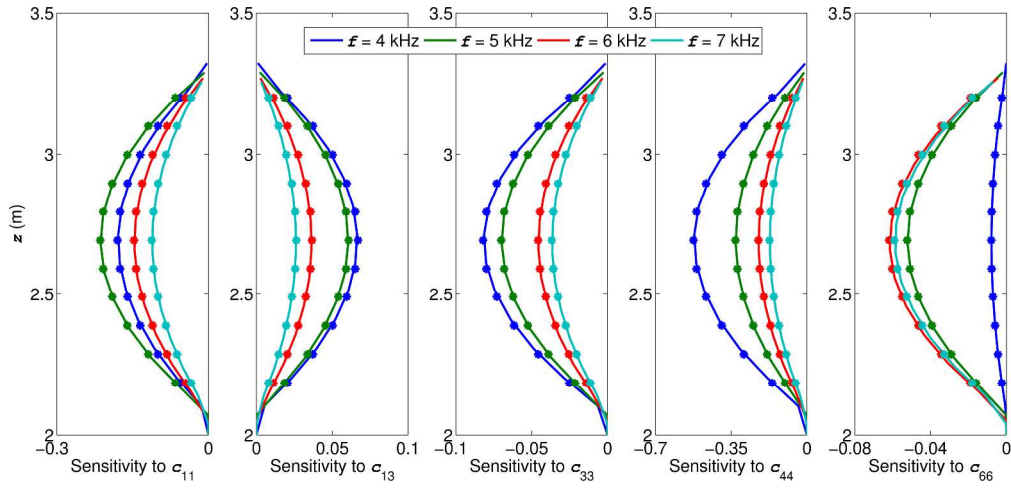


Figure A2

332x156mm (300 x 300 DPI)

1  
2  
3  
4  
5  
6  
7  
8  
9  
10  
11  
12  
13  
14  
15  
16  
17  
18  
19  
20  
21  
22  
23  
24  
25  
26  
27  
28  
29  
30  
31  
32  
33  
34  
35  
36  
37  
38  
39  
40  
41  
42  
43  
44  
45  
46  
47  
48  
49  
50  
51  
52  
53  
54  
55  
56  
57  
58  
59  
60

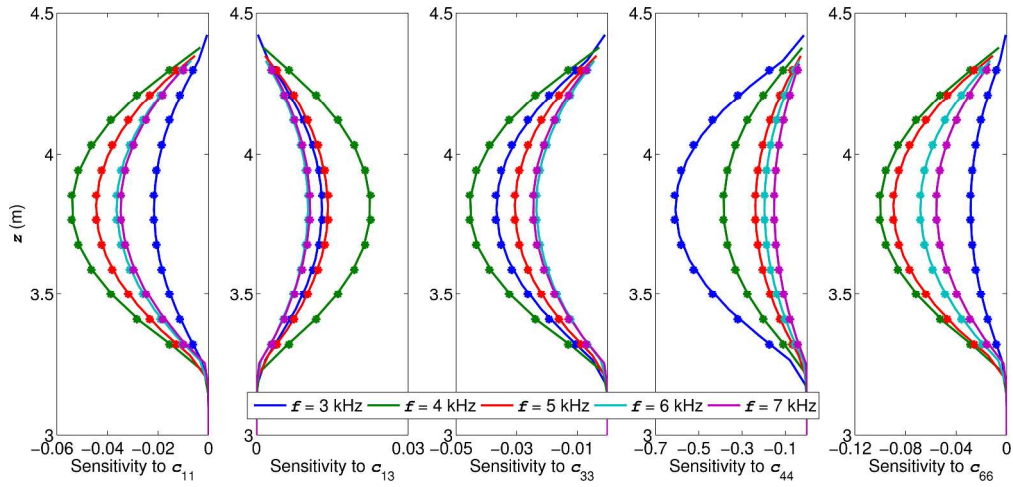


Figure A3

332x156mm (300 x 300 DPI)

## DATA AND MATERIALS AVAILABILITY

Data associated with this research are available and can be obtained by contacting the corresponding author.